

Electronic Theses and Dissertations, 2004-2019

2018

The Study of an Impinging Unsteady Jet - Fluid Mechanics and Heat Transfer Analysis

Andrea Osorio

 Part of the [Biomechanical Engineering Commons](#)
Find similar works at: <https://stars.library.ucf.edu/etd>
University of Central Florida Libraries <http://library.ucf.edu>

This Masters Thesis (Open Access) is brought to you for free and open access by STARS. It has been accepted for inclusion in Electronic Theses and Dissertations, 2004-2019 by an authorized administrator of STARS. For more information, please contact STARS@ucf.edu.

STARS Citation

Osorio, Andrea, "The Study of an Impinging Unsteady Jet - Fluid Mechanics and Heat Transfer Analysis" (2018). *Electronic Theses and Dissertations, 2004-2019*. 6208.
<https://stars.library.ucf.edu/etd/6208>

THE STUDY OF AN IMPINGING UNSTEADY JET - FLUID MECHANICS AND HEAT
TRANSFER ANALYSIS

by

ANDREA OSORIO

B.S. Mechanical Engineering, University of Central Florida, 2016

A thesis submitted in partial fulfilment of the requirements
for the degree of Master of Science in Mechanical Engineering
in the Department of Mechanical and Aerospace Engineering
in the College of Engineering and Computer Science
at the University of Central Florida
Orlando, Florida

Fall Term
2018

© 2018 Andrea Osorio

ABSTRACT

The high heat transfer capabilities of impinging jets have led to their widespread use in industrial applications, such as gas turbine cooling. These impinging jets are usually manufactured on the walls of super-alloy metals and are influenced by being positioned with a confined setting. Studies have been shown to enhance the heat transfer of impinging jets by fluctuating the flow which will be analyzed in this project with two designs. The first design is a self-sustaining stationary fluidic oscillator that causes a sweeping motion jet to impinge on the surface. This is investigated using Particle Image Velocimetry (PIV) to study the flow field as well as copper-block heated surface to study the heat transfer. The second design involves pulsating the jet through a rotating disk that opens and closes the jet hole, providing a pulsing impingement on the surface. This is examined using hot-wire anemometry for understanding the fluid mechanics and copper-block heated surface to study the heat transfer. Both configurations are tested at a constant Reynolds number of 30,000 with the oscillator tested at normalized jet-to-surface spacings of 3, 4, 6 and the pulsing mechanism tested at jet-to-surface spacing of 3. The results for the fluidic oscillator indicate: Reynolds stress profiles of the jet demonstrated elevated levels of mixing for the fluidic oscillator; heat transfer enhancement was seen in some cases; a confined jet does worse than an unconfined case; and the oscillator's heat removal performed best at lower jet-to-surface spacings. The results for the pulsing mechanism indicate: lower frequencies displayed high turbulence right at the exit of the jet as well as the jet-to-surface spacing of 3; the duty cycle parameter strongly influences the heat transfer results; and heat transfer enhancement was seen for a variation of frequencies.

To my parents who love me unconditionally and dedicated their lives to provide me a prosperous future.

ACKNOWLEDGMENTS

Thank God for He has done great things in my life. I'd like to thank family, particularly my sister, for supporting me and guiding me throughout my time in school. Many thanks to Siemens, specifically Dr. Rodriguez, for allowing me to pursue this work and supporting this project. Thank you Dr. Kapat for providing the essential tools that allowed me to finish my thesis work. To my colleagues who helped me to learn all that I know about research - I cannot thank you enough for assisting me with finishing this work. It has been a learning experience that I will always treasure.

TABLE OF CONTENTS

LIST OF FIGURES	viii
LIST OF TABLES	xi
NOMENCLATURE	xii
CHAPTER 1: INTRODUCTION	1
1.1 Gas Turbine Cooling	1
CHAPTER 2: BACKGROUND	4
2.1 Steady Impinging Jets	4
2.2 Fluidic Oscillator Review	6
2.3 Pulsating Flow Review	9
CHAPTER 3: MEASUREMENT TECHNIQUE	14
3.1 Flow Measurements Experiments	14
3.1.1 Particle Image Velocimetry Background and Description	14
3.1.2 Hot-Wire Background and Description	16
3.2 Heat Transfer Experiments	19
3.2.1 Temperature Measurements	22
3.2.2 Mass Flow Measurements	26
3.2.3 Heat Leakage	26
3.2.4 Addition of Fluidic Oscillator	27
3.2.5 Addition of Pulsing Mechanism	28
3.3 Uncertainty	32

CHAPTER 4: ANALYSIS OF FLUIDIC OSCILLATOR	35
4.1 Flow Analysis Results	36
4.1.1 PIV Confined/Unconfined Mean Velocity Fields	36
4.1.2 PIV Boundary Layer Confined/Unconfined Comparison	40
4.1.3 PIV Confined Reynolds Stresses	43
4.2 Heat Transfer Results	45
4.3 Summary of the Results	48
CHAPTER 5: ANALYSIS OF PULSING MECHANISM	50
5.1 Flow Analysis Results	50
5.1.1 Mean Velocity and Turbulence	51
5.1.2 Duty Cycle - DC	54
5.1.3 Power Spectral Density - PSD	61
5.2 Heat Transfer Results	71
5.2.1 Additional Heat Transfer Data	75
5.3 Summary of the Results	79
CHAPTER 6: CONCLUDING REMARKS AND FUTURE WORK	81
LIST OF REFERENCES	82

LIST OF FIGURES

Figure 1.1: Impingement in Turbine Blade [2]	2
Figure 1.2: Flow Region of Impinging Jet, [15]	3
Figure 2.1: Nusselt Number Profiles when Varying Jet-to-Surface Spacings	5
Figure 2.2: Fluidic Oscillator Design [40]	6
Figure 3.1: Energy Balance of a Small Element	16
Figure 3.2: Wheatstone Bridge for a Constant Temperature Anemometer	18
Figure 3.3: Isometric View of Heat Transfer Rig	20
Figure 3.4: Section Cut View of the Rig Where the Top Acrylic Lid (A) and Side Chamber Walls (B)	21
Figure 3.5: Alternative Views to the Acrylic Top Lid and the Chamber Side walls from Figure 3.4	22
Figure 3.6: Temperature Measurements Within the Rig	24
Figure 3.7: Sample Measurement Planes Section A and B for the TCs Within the Copper Test Articles	25
Figure 3.8: Fluidic Oscillator Setup	28
Figure 3.9: Pulsed Setup	29
Figure 3.10: Pulsed Setup - Plenum and Articles	30
Figure 3.11: DC Disks: 27% (left), 33%(center), and 50% (right)	31
Figure 3.12: Uncertainty Tree - Reynolds Number	33
Figure 3.13: Uncertainty Tree - Nusselt Number	34
Figure 4.1: Mean Velocity Fields for Different $z/d = 2, 3, 4, 6$ (top to bottom) and Confined (left) and Unconfined (right), Respectively.	38

Figure 4.2:	Non-Dimensionalized Velocity Plotted at $z/d=1$ for $z/d=2,3,4,6$ for Baseline (left) and Fluidic Oscillator (right)	39
Figure 4.3:	Wall Jet Velocity Profiles for Baseline and FO at $z/d=2$	40
Figure 4.4:	Boundary Layer Locations Where (a.) is $r/d = 1$, (b.) is $r/d = 2$, (c.) is $r/d=3$, and (d.) is $r/d=4$	41
Figure 4.5:	Boundary Layer Profile at Various Streamwise Locations for Confined Case, $r/d = 1$ (Top Left), $r/d = 2$ (Top Right), $r/d = 3$ (Bottom Left), $r/d = 4$ (Bottom Right)	42
Figure 4.6:	Boundary Layer Profiles Comparison for Confined (C) and Unconfined (UC) at Various Radial Locations for $z/d=4$ (Left) and $z/d=6$ (Right)	43
Figure 4.7:	Reynolds Stresses for Baseline (Top) and Fluidic Oscillator (Bottom) for $z/d=2,3,4,6$ (Left to Right)	44
Figure 4.8:	Reynolds Stresses, uv , Plotted at $z/d = 1$ for $z/d = 2,3,4,6$ for Baseline (Left) and FO (Right)	45
Figure 4.9:	Normalized Nusselt Number for Baseline and Fluidic Oscillator for Confined Setup	47
Figure 4.10:	Normalized Nusselt Number for Baseline and Fluidic Oscillator for Unconfined Setup	47
Figure 5.1:	Strouhal Numbers for DC=27%, 33%, 50%	52
Figure 5.2:	Mean Velocity for Reynolds Number=30,000 and $z/d=0$ for DC=27%, 33%, 50%	53
Figure 5.3:	Root Mean Square of Mean Velocity for DC=27%, 33%, 50%	54
Figure 5.4:	Opening Area Change During a Period. Shaded Circle: Jet Opening ; Open Circle: Disk Opening	55
Figure 5.5:	DC of 27% at a Frequency of 20 Hz	57

Figure 5.6: DC of 27% at a Frequency of 400 Hz	57
Figure 5.7: DC of 33% at a Frequency of 20 Hz	58
Figure 5.8: DC of 33% at a Frequency of 400 Hz	59
Figure 5.9: DC of 50% at a Frequency of 20 Hz	60
Figure 5.10: DC of 50% at a Frequency of 400 Hz	60
Figure 5.11: PSD of Steady Jet at a $z/d=0$	62
Figure 5.12: PSD of Steady Jet at a $z/d=3$	63
Figure 5.13: PSD for Frequencies of 20 Hz, 50 Hz, 100 Hz for a DC of 27%	65
Figure 5.14: PSD for Frequencies of 200 Hz, 300 Hz, 400 Hz for a DC of 27%	66
Figure 5.15: PSD for Frequencies of 20 Hz, 50 Hz, 100 Hz for a DC of 33%	67
Figure 5.16: PSD for Frequencies of 200 Hz, 300 Hz, 400 Hz for a DC of 33%	68
Figure 5.17: PSD for Frequencies of 20 Hz, 50 Hz, 100 Hz for a DC = 50%	69
Figure 5.18: PSD for Frequencies of 200 Hz, 300 Hz, 400 Hz for a DC = 50%	70
Figure 5.19: PSD for Frequencies of 20 Hz, 50 Hz, 100 Hz for a DC = 27% at a $z/d=3$	71
Figure 5.20: PSD for Frequencies of 200 Hz, 300 Hz, 400 Hz for a DC = 27% at a $z/d=3$	72
Figure 5.21: PSD for Frequencies of 20 Hz, 50 Hz, 100 Hz for a DC = 33% at a $z/d=3$	73
Figure 5.22: PSD for Frequencies of 200 Hz, 300 Hz, 400 Hz for a DC = 33% at a $z/d=3$	74
Figure 5.23: PSD for Frequencies of 20 Hz, 50 Hz, 100 Hz for a DC = 50% at a $z/d=3$	75
Figure 5.24: PSD for Frequencies of 200 Hz, 300 Hz, 400 Hz for a DC = 50% at a $z/d=3$	76
Figure 5.25: Nusselt Number Comparison of Baseline and DC = 27%	76
Figure 5.26: Nusselt Number Comparison of Baseline and DC = 33%	77
Figure 5.27: Nusselt Number Comparison of Baseline and DC = 50%	77
Figure 5.28: Nusselt Number Comparison of Baseline and DC = 50% for a Reynolds Number = 34,000 and $z/d=2$	78

LIST OF TABLES

Table 2.1:	Fluidic Oscillator Studies	7
Table 2.2:	Pulsing Mechanism Studies	11
Table 3.1:	Testing Matrix	14
Table 3.2:	Uncertainty	32
Table 4.1:	Fluidic Oscillator Design Parameters	35
Table 4.2:	Fluidic Oscillator Flow Analysis Matrix	36
Table 4.3:	Fluidic Oscillator Heat Transfer Matrix	46
Table 5.1:	Pulsing Mechanism Matrix	50
Table 5.2:	Pulsed Flow Heat Transfer Test Matrix	72

NOMENCLATURE

\bar{U}	Mean Velocity [m/s]
\dot{m}	Mass Flow Rate [kg/s]
\dot{Q}_c	Conductive Heat Generation Rate [W]
\dot{Q}_e	Electrical Heat Generation Rate [W]
\dot{Q}_r	Radiative Heat Generation Rate [W]
\dot{Q}_s	Heat Storage Rate [W]
\dot{Q}_{fc}	Forced Convective Heat Generation Rate [W]
\dot{V}	Volume Flow Rate
A_w	Wire Cross-Sectional Area [m^2]
B	Baseline Condition
C	Confined Condition
D	Surface Diameter [m]
d	Jet Diameter [m]
DC	Duty Cycle [%]
DMD	Dynamic Mode Decomposition
E	Anemometer Output Voltage

e fluctuating anemometer voltage

E_t Theoretical Wire Voltage

e_{off} Amplifier Offset Voltage

f Frequency [Hz]

FDX Fluid Dynamix

FFT Fast Fourier Transform

G Gain of Amplifier in Anemometer

h Heat Transfer Coefficient [$W/(m^2K)$]

HWA Hot-Wire Anemometry

I Current [A]

k Thermal Conductivity [$W/(mK)$]

L Length of Nozzle [m] or Length of Signal

l Longitudinal Integral Length Scale [m]

LDV Laser Doppler Velocimetry

N Number of Samples in a Time-History Record

P Pressure [Pa]

PIV Particle Image Velocimetry

POD Proper Orthogonal Decomposition

PSP Pressure Sensitive Paint

R Gas Constant

r Radius of Disk [m]

R_1, R_2, R_3 Resistors in Wheatstone Bridge

R_L Resistance of Probe Lead and Cables

R_w Resistance of Heated Wire at Temperature, T_w

Re Reynolds Number

RIT Rotor Inlet Temperature

Sr Strouhal Number

T Temperature

T_a Temperature of Ambient Fluid

T_w Temperature of Heated Wire

TBC Thermal Barrier Coating

TC Thermocouple

Tu Turbulence Intensity

U Velocity

u, v, w All Components of Velocity

UC Unconfined Condition

uv Reynolds Stress Components of Velocity in a 1-D Plane

VFD Variable Frequency Drive

z Jet to Surface Length [m]

z/d Jet-To-Surface Spacing

Greek Symbols

χ Resistivity

Δ Change in Value

∞ Free-Stream Conditions

μ Dynamic Viscosity [$(Ns)/m^2$]

ρ Density [kg/m^3]

Superscripts and Subscripts

' RMS Value

0 Stagnation Point on Surface

- Time-Mean Value

amb Ambient Conditions

avg Average Reading

c Conduction

e Electrical

fc Forced Convection

fluid Average Value of Fluid

i component

jet Jet Hole

max Maximum Value of Jet

out Related to the Disk [*m*]

r Radiative

rms Root Mean Square

s Storage or Sampling

surface Copper Block Surface

w Reference Conditions

CHAPTER 1: INTRODUCTION

The motivation for this research was provided by a Siemens project at the University of Central Florida lead towards understanding fluctuating impingement flow with the focus for turbine blade cooling. The main objective of this project was to initiate the understanding of unsteady jet flow and the impacts on heat transfer. The current work is a summary of two methods used to fluctuate the flow and summarize the fluid behavior and heat transfer results.

1.1 Gas Turbine Cooling

Gas turbines are used in land-based power generation and aircraft propulsion. When increasing the turbine rotor inlet temperatures, the power output and thermal efficiency increase. This drives the increase the rotor inlet temperature (RIT) has provided for researching high-temperature materials such as thermal barrier coating (TBC) and sophisticated internal cooling schemes which permits for the blades to withstand the significantly higher RIT. Most of the research done for gas turbines is directed to improve what was stated before and to increase the flow path efficiency with reduced leakage [16]. The fluid within a gas turbine engine directly correlates to the power derived from the chemical energy and the methods of containing the energy [2]. The flow path leads to the fan, compressor, turbine, and then exhaust. As the flow is dispersed in the turbine, the compressor bleed flow is directed for cooling the turbine blades where high temperatures from the combustor fluid entering affects the first stage blades. The focus of the current research is in a small section of the blade at the leading edge of the blade where the temperature is relatively the highest as shown in Figure 1. This section of the blade is cooled by a method called jet impingement. Jet impingement cooling can be described as the exhausting cool air from a jet hole that impinges on to a hot surface. The benefits of impingement are the high speed jets that are guided to the inner surface to remove high loads of heat and it is a flexible method

that allows for a composition of arrays of jets. The general goals are defined by the amount of flow exiting the jet, the pressure drop of the jet, and the amount of heat removed from the surface.

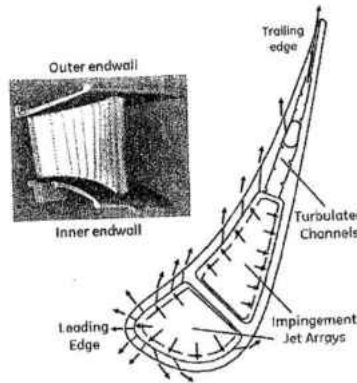


Figure 1.1: Impingement in Turbine Blade [2]

Although the motivation for this work is specific to cooling the interior surfaces of turbine blades, it can be applied in the combustor liners, HPT vanes, shrouds, among others within a turbine Amano (2014). It has been used in applications such as cooling of electronic components, manufacture of printed wire boards and metal sheets, thermal drying of continuous sheet of materials (lumber, veneer, papers, films, textiles, etc.), de-icing of air craft wings, printing processes, drying of foods, and tempering of glass and nonferrous metal sheets [12].

One method to expand on the impingement technique is to excite the jet causing it to be unsteady through variable pressure differentials. This has been studied for the past five decades with divergent and contradictory results as new research techniques enable to characterize the flow [46]. Fluctuating the flow is defined as a transient case where the flow field alters with time. This results in understanding the characteristics of the flow as it fluctuates and explaining the fluid mechanics as well as the heat removal. In the present study, the knowledge from a steady jet is expanded to contrast with unsteady impingement by adding more parameters to analyze its effects on heat transfer.

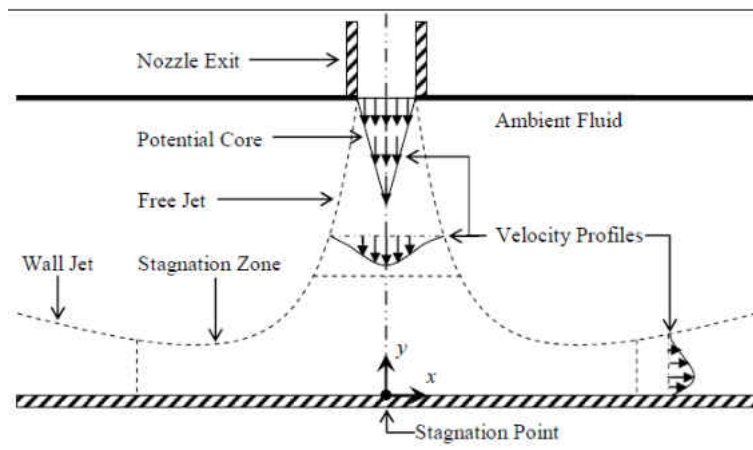


Figure 1.2: Flow Region of Impinging Jet, [15]

CHAPTER 2: BACKGROUND

A directed jet is a flexible and effective method to transfer mass or energy in industrial applications. Prior to the design of an impinging jet, the flow rate is characterized by the Reynolds number and the heat transfer by the Nusselt number as non-dimensional terms. Further terms are included when studying a transient flow that will be further discussed later. Moreover, the timeline presented for this work allowed for two techniques to be studied and further study will involve relating both techniques to optimize heat transfer for a set of parameters. The first section discusses would be to use a self-oscillating sweeping jet known as a fluidic oscillator. The second section discusses a flow that is broken known as pulsing flow. Both systems will be studied from the flow field and heat transfer standpoints.

2.1 Steady Impinging Jets

To understand how the unsteady jet came into consideration, an analysis on impingement flow will describe the fundamentals of the technique. The terms generally associated with impingement flow are given by Han [15] in Figure 2.1 where the regions of studied are: the potential core, free jet, stagnation region, and wall jet. The flow exiting from the nozzle streams towards the surface and mixes with the ambient fluid interim. This momentum trade narrows down the potential core as the ambient flow and jet produce a thin layer of mixing known as the shear layer. The velocity profile then branches out as the flow moves downstream of the nozzle. The spacing between the jet and surface will be given the nomenclature z/d where z is the y naming in Figure 2.1 and d is the jet diameter at the exit. If the z/d is large enough, the potential will conclude before reaching the stagnation region. This potential core typically is 5 to 10 nozzle diameters in length [25]. The confined plate is located right at the exit of the jet where the flow circulating around the jet is restricted from rising above the nozzle. This is considered for applications such as a turbine blade

where the flow exiting is led towards more cooling holes. There is also a region immediately after the stagnation area known as the deflection zone where the axial velocity slows down significantly therefore a rise in static pressure. After that is the wall jet where the heat removal continues as the flow accelerates and is parallel to the heated surface where a boundary layer forms. As the flow spreads radially, the boundary layer mixes with the stationary ambient fluid slowing down the flow. The Nusselt number variation as seen in Figure 2.1, where an illustration of local Nusselt number from the stagnation region radially outwards is plotted. The second peak shown as a dashed line occurs from the sudden rise in turbulence from the stream wise pressure gradient explained by Martin [32]. Another explanation comes from the vortices form in the shear layer of the jet known as the Kelvin-Helmholtz instability. The large scale vortices impinge on the surface and enhances the entrainment speed and mixing process. Visual images are presented by Popiel [39] where a “roll up” of the vortices on the surface can explain the additional heat transfer enhancement.

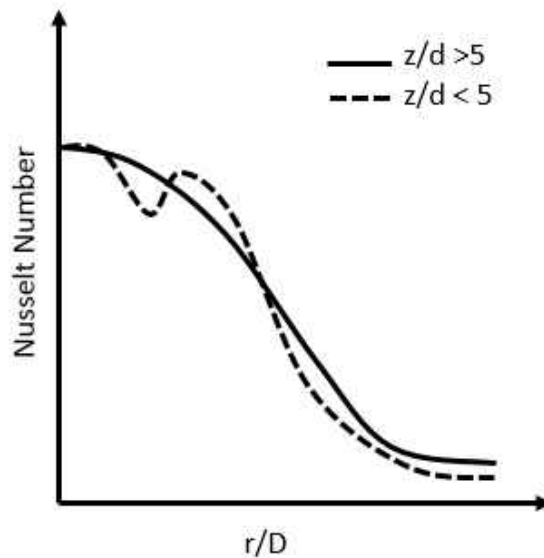


Figure 2.1: Nusselt Number Profiles when Varying Jet-to-Surface Spacings

2.2 Fluidic Oscillator Review

The interest for fluidic oscillators was presented in the aerodynamic community for flow control where the idea of non-moving parts attracted much attention. Varying the design of the oscillator brought along the study of its applications where a historical development is discussed by Gregory [13]. The fluidic instabilities produced from the oscillators has brought a curiosity of its impact on heat transfer. The current study characterizes the design of the fluidic oscillator and the difference in heat removal to a steady jet.

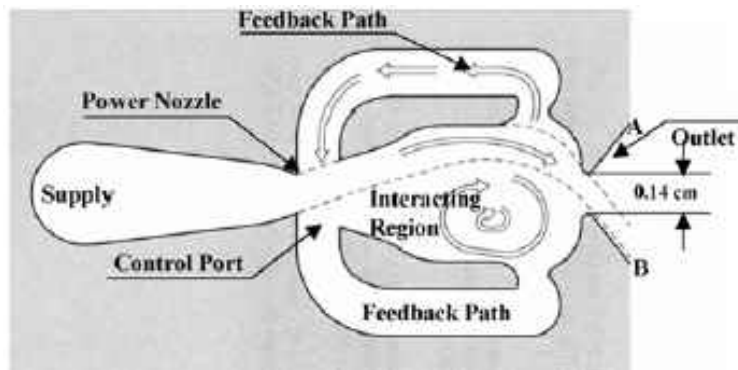


Figure 2.2: Fluidic Oscillator Design [40]

The fluidic oscillator is described by the Coanda effect where a turbulent jet entrains flow as it enters a device. The entrained flow is restricted by a wall within a device and the jet decreases the static pressure between the wall and jet. This pressure difference attracts the jet towards a curved wall. With the jet deflecting towards the curved wall, the pressure drop increases and the entrained flow is further restricted. The entrained flow is then guided through channels; the pressure difference induces the flow to mix again with the turbulent jet where the pattern is repeated. This produces a time-dependent flow where the jet exhibits a sweeping motion thus called a sweeping jet. The required detachment pressure is dependent on the angle and curvature of the walls resulting in the frequency of jet at the exit.

Table 2.1: Fluidic Oscillator Studies

Fluidic Oscillator Studies					
[Paper Number] Author, Year	Reynolds Number (Nozzle Height Range)	Frequency (Hz)	Spreading Angle (°)	Data	Measurement Technique
[7] Camci, 2002	7500-14000 (24-60)	20-100	40	Nu	Constant Temperature Anemometer Heated Surface
[33] Narumanchi, 2008	-	100-700	30-60	htc	Heated Surface
[1] Agricola, 2017	20000-35000 (5-7)	100-1000	70, 102	Nu_{local} ; Flow Field	IR Thermography; Heated Surface
[22] Hossain, 2017	-	30-1000	36, 60	Flow Field	Schlieren Image; Numerical Study
[30] Lundgreen, 2017	(3, 4, 6, 8)	678	49-78	Nu/Re0.72	Numerical Study
[10] Demircan, 2010	100-700	3-10	-	Nu_{local}	Numerical Study
[35] Ostermann, 2015	0-60000	0-20	-	Flow Field	Particle Image Velocimetry
[17] Herr, 1994	-	10-100	-	Flow Field	Hot Wire
[40] Raman, 2014	-	0 – 3000	-	Flow Field	Schlieren Image
[36] Page, 1995	150000 (6.35)	5000	-	Nu_{local}	Heated Surface
[14] Gregory, 2007	2700	6000-22000	-	Flow Field	Pressure Sensitive Paint; Water Visualization
[45] Wen, 2018	2700-9300 (8)	333-500	81	Flow Field	Particle Image Velocimetry

The angle of the exiting jet is commonly known as the spreading angle. Studies have been conducted to isolate each of the parameters of a fluidic oscillator to vary the strength of the jet [36]. Table 2.1 considers a short summary of papers reviewed when considering the design of the fluidic oscillator.

With the application of fluidic oscillators used for flow control, most research done has been to understand the flow field. Papers such as Narumanchi [33], Raman [40], and Viets [43] focus on the parasitic power, cavity tone suppression, and thrust augmenting ejector effect, respectively. Camci [7] noticed a variation in frequency by adjusting the length and diameter of the power nozzle and the stagnation pressure of the plenum chamber. The sweeping of the jet increases the convection and diffusion considerably while the kinetic energy is unaltered. Hossain [22] noted the effects of roughness within the internal structure of the fluidic oscillator to the oscillation frequency and spreading angle. The conclusion being that roughness increases the effective aspect ratio of the oscillator resulting in an increase in frequency of the jet. Also, the spreading angle decreases

when roughness produces an earlier transition of the laminar separation bubble. The last main point being the most detrimental from roughness is the main mixing channel.

Ostermann [35] compared the internal and external designs of two oscillator designs. It was noted that the angle and curvature of the oscillator affected the pressure drop within the oscillator. The external flow field showed different sweeping angles solely based on the internal design of the oscillators. Another conclusion was the higher entrainment effects of the fluidic oscillator compared to a steady jet. Herr [17] isolated the contributions of the turbulent fluctuations and deterministic oscillations on the momentum heat transfer process. One of the conclusions from the hot-wire data showed both turbulence and oscillation stresses for the specific unsteady flow are smaller than the turbulence stresses of a steady jet. Another being the oscillation enhances transport process because of the existence of additional inertia forces and additional thermal fluxes (also known as the oscillation heat flux). The unsteady jet's kinetic energy magnitude due to oscillations is about typically three times of that due to turbulence.

Bobusch [5] performed a Proper Orthogonal Decomposition (POD) method to illustrate a detailed flow structures during the oscillating process within the oscillator to understand how to attain optimal performance. One main point was the ability to change the frequency of the oscillator by adjusting the flow rate within both feedback channels. Gregory [14] tested microfluidic oscillators for the use of flow control with pressure sensitive paint (PSP) and microphones to characterize the flow field and power spectra, respectively. The jet oscillated at a frequency ranging from 6 to 22 kHz. It was found that the variation of frequency with flow rate was linear with a slight varied slope that occurred from the turbulent noise. The oscillations in the linear region displayed a triangular wave with rich high frequency; any oscillations after that, above the discontinuity, were closer to a sinusoidal wave. Wen [45] investigated the flow field of a fluidic oscillator using Particle Image Velocimetry (PIV) at varying Reynolds number to see the variations in frequency. It was noted that an approximately linear increase was seen of sweeping frequency versus Reynolds number.

Agricola [1] studied the effects on heat transfer and a visual image of the jet impingement on the surface. It was verified that the jet-to-surface spacing for the maximum impingement enhancement of a sweeping jet varies from the maximum impingement enhancement from a circular jet due to the dependence of the sweeping jet exit nozzle angle. It was noted that the frequency of oscillation was highly dependent on: mass flow rate, length of feedback channels, and the temperature of the fluid. The strength and frequency of oscillation increases with reducing the exit nozzle angle. Also, the spreading angle made small enough for the jet to attach to the walls will form a heat transfer profile with two distinct lobes and produce higher heat transfer. Lundgreen [30] studied the same sweeping jet with varying mass flow rate and jet-to-surface spacings. The heat transfer performance decreased for higher jet-to-surface spacings like a steady jet while a more uniform heat removal on the surface was noticed.

Demircan [10] did a numerical study of a sinusoidal jet oscillator for a Reynolds number of 100-700. It was observed that the local Nusselt number is maximum at the impingement point and decreases along the plate. The usual monotonic decreasing behavior of a steady jet was not seen for a sweeping jet. There were local maxima and minima values because of the recirculating flow above the boundary layer. Increasing the oscillation frequency correlated to an increase in local Nusselt number at the stagnation region up to a certain frequency. After that frequency, the Nusselt number remained the same. Page [36] conducted a straightforward study of an extended nozzle with angled walls at the entrance. It was noticed that an enhancement was seen with two designs of the self-oscillating mechanism relative a steady jet. A first-stage frequency of 5,000 Hz with strong harmonics in the ultrasonic range were exhibited by the oscillator.

2.3 Pulsating Flow Review

The idea of an unsteady jet can be performed in several manners with another method involving breaking the jet to create a pulsing action. In the case of considering it for a turbine

blade, it is unrealistic to add a device that could clog and alter its purpose. Thus, the gist of using a pulsing mechanism was to replicate the pulsing characteristic to the flow and use the data to eventually design the jet to imitate this behavior. Several iterations were used to develop a design that would currently fit into the heat transfer rig provided by Siemens. The main requirements when discussing the setups would be:

- Determined Reynolds Number
- Determined jet-to-surface spacing (z/d)
- Vary the pulsing frequency (also a parameter in the Strouhal number)
- Involve a confinement plate
- Cost of the final design

The final design was flexible with all these requirements as well as varying the amplitude of the flow. This was done by considering the amount of flow exiting the jet at a given time which generally is called the duty cycle. A typical non-dimensional term that explains the mechanism of oscillating flow is the Strouhal number given in equation 2.1 where f is the frequency, d is the jet diameter, and \bar{U} is the mean velocity.

$$Sr = \frac{fd}{\bar{U}} \quad (2.1)$$

Table 2.2: Pulsing Mechanism Studies

Pulsation Mechanism Studies					
[Paper Number] Author, Year	Nozzle Type	Reynolds Number (z/d)	Frequency (Hz)	Data	Measurement Technique
[21] Hofmann, 2007	Nozzle shape	14000-78000 (2, 5, 8.5)	1-59	Nu_{local}	Thermography; LDV
[37] Persoons, 2013	Sharp Pipe Nozzle	6000-14000 (1-6)	9-55	Nu_{local}	Copper block
[27] Janetzke, 2009	Pipe Nozzle L/d=2.5	7,280 (0-2)	0-700	Flow Field	PIV; Surface Hot Wire
[26] Janetzke, 2008	Pipe Nozzle L/d =2.5	7,280 (0-2)	0-700	Nu_0	PIV; Heated Plate; Oil Film
[41] Sailor, 1999	Pipe Nozzle L/d =3.6	21000-31000 (4, 6, 8)	20-60	Nu_{avg}	Thermal Anemometer; HWA
[8] Choutapalli, 2009	Contoured Pipe Nozzle	340000	-	Flow Field	PIV
[42] Sheriff & Zumbrunnen, 1999	Orifice	2500-10000 (2-6)	0-65	Nu_{local}	Hot Film Anemometer; Heat Flux Microsensor
[47] Zulkifli, 2007	Orifice	16000-32000 (4)	10-80	Nu_{local}	Heat Flux; HWA

Designs considered were the butterfly valve by Kimura, Herr, Wang, and Huang [28], [17], [44], [23] respectively. Other designs such as the solenoid valve were thought of [31]. The final design was inspired by Choutapalli who used it for the study of turbulent pulsed air for thrust augmentation [8]. While the motivation afterwards was to validate the heat transfer results with prior work, it was difficult to find a study similar to the general parameters given with the rig and timeline. The papers closest to the design of a pulsing flow were Hofmann [21] and Zulkifli [47]. Hofmann [20] created periodic fluctuations to the mean flow while Zulkifli [47] used a rotating cylinder to pulse the jet. These ideas were studied to analyze how to pulse the flow as well as the frequencies of interest which will be discussed later.

Esmailpour [12] demonstrated how the cooling performance increases with amplitude and frequency of the pulsation which occurs at smaller jet-to-nozzle spacing. To quantify the pulsing mechanism, the Sr number is used as a non-dimensional representation of frequency for a given speed and length scale. Esmailpour obtained the highest enhancement of heat transfer (13%) at Sr of 0.26 for a jet-to-nozzle spacing of 2. Hofmann [21] combined a mean steady flow with a periodic part. A correlation between the quasi-steady behaviors of a jet up to a Sr number of 0.2

demonstrated the amplitude of the pulsation performance being similar to a steady jet; a correlation for Nusselt number as a function of Re number and Prandtl number was generated [20]. The jet was shown to become broader and the core jet length to be smaller with the pulsation; also the heat transfer increased when the shear surface of the jet is large enough to enable mixing down the centerline. Due to the mixing of the pulsating flow and the surrounding air, the difference between the jet temperature and impingement plate temperature decreases as the pulsation amplitude is increased. Another observation was seen at low jet-to-surface spacing where the effects of entrainment and lower jet velocity did not significantly influence the jet core. An evaluation of the data expressed that heat transfer can be affected by pulsation when the frequency of the pulsation has the same order of magnitude as the vortex frequency of the turbulence. This vortex frequency is created at the boundary of the nozzle and transported along the jet. The mixing effect occurs when the residence time – calculated as the time from the exit of the nozzle to the tip of the core jet – is less than the period of the vortex.

Persoons [38] noticed a breakup of the thermal boundary layer with synthetic jets while steady jets produce thin boundary layers. The solenoid pulsation flow appeared to be affecting the heat transfer more in the wall jet region rather than the stagnation zone. An area-averaged enhancement of up to 85% was seen for a jet-to-nozzle spacing of 6, frequency of 55Hz and Reynolds number of 6,000 with a Strouhal number of 0.2. Janetzke [26] and [27], varied the frequency while keeping a constant flow rate for 3 submerged jets. The vortex rings were tracked to determine its impact on heat transfer. It was noted that a strong vortex at the wall would induce a secondary smaller counter rotating vortex followed by the two vortices merging. The maximum vortex strength appeared to be when the jet was excited to a Sr number of 0.82 and high amplitudes where the vortex pairing occurred and maximum wall shear stresses. The size and strength of the vortices reduced for lower Sr numbers. The reinforcement of the Kelvin-Helmholtz vortices in the jet shear layer was influenced by the Sr number and the pulsation magnitude. These vortices interrupt the boundary layer process at the surface that showed a stagnation heat transfer

enhancement of up to 20%.

Sailor [41] varied the pulsation amplitude by varying the duty cycle which is the ratio of on-time to total cycle time. This is varied by the area of the air passage created by the valve. Heat transfer enhancement was believed to occur from the secondary vortices impinging on the heated surface. A nominal Reynolds number was calculated from the average centerline velocities for both steady and pulsating flow. A maximum heat transfer of 65% occurred for a Reynolds number of 31,000, $z/d = 4$, and duty cycle (DC) of 25%. Choutapalli focused on the flow structures of a pulsating flow with a duty cycle of 50% where the goal of this work was to augment the thrust for short-duration vertical flight - [8] and [9]. It was noted how higher Sr numbers had closely spaced vortex rings and a distinct region of jet flow appear for lower Sr numbers. With that being said, the optimum combination of spacing and strength seemed to occur at a Sr number of 0.24. The Sr number induced the entrainment, mass flux, and momentum flux effects.

Sheriff and Zumbrunnen [42] explored the effects of pulsating flow on an array of jet where a decrement of 18% was seen at the stagnation region. It was noted that secondary vortices were not formed for z/d values (normalized jet-to-surface spacings) greater than 6. The turbulent intensities, nonetheless, were 7-15% higher than the steady jet array values close to the surface. A high heat removal at the stagnation point was decreased with pulsation where a uniform heat transfer rate was observed which can be useful in many applications. Zulkifli [47] and [48] studied the effects of varying frequencies and Reynolds number at jet-to-surface spacing of 4. The observation from the data was an enhancement for every frequency due to higher localized heat transfer. The heat transfer measurement was taken radially where a higher instantaneous velocity was observed. Several main conclusions from these papers and others were taken into account. As the heat transfer results vary greatly with pulsating flow, a deeper look into two parameters will be of focus. The main results taken into consideration was the pulsating amplitude that will later be measured using a duty cycle disk and the frequency which will be controlled with a variable-frequency drive.

CHAPTER 3: MEASUREMENT TECHNIQUE

With the available tools from Siemens at the Siemens Energy Center, the study of the flow field and heat transfer were readily available. The current rig used for the heat transfer experiment had been established and studied for some time. To gather more information on test cases with the heat transfer rig, refer to Hodges [19]. Table 3.1 categorizes the template of this work where the Reynolds number is constant at 30,000.

Table 3.1: Testing Matrix

Testing Matrix	PIV	Hot-Wire	Heat Transfer	Confined (C)	Unconfined (UC)	Changes in z/d
Fluidic Oscillator	✓		✓	✓	✓	✓
Pulsed Flow		✓	✓	✓		

3.1 Flow Measurements Experiments

To understand the fluidic oscillator and pulsating mechanism, the techniques used for both were altered. In terms of the fluidic oscillator, the flow field, Reynolds Stresses, and boundary layer for various jet-to-surface spacings. In terms of the pulsing mechanism, the jet exit mean velocities, duty cycle, and energy spectrum were studied. The general idea of pulsating mechanism was to gather information of the effects of frequency and duty cycle on the flow. Since a realistic design that produces an unsteady jet should not involve moving parts, the pulsating flow was meant to first inspect if there would be heat transfer enhancement to a steady jet.

3.1.1 Particle Image Velocimetry Background and Description

To understand the flow behaviour at the affected surface of the fluidic oscillator, the flow field was studied using Particle Image Velocimetry (PIV). PIV is an optical method of flow visualization

to gather instantaneous velocity measurements that may be time-resolved in an area or volume. This study involved time-resolved velocity images about a single plane parallel to the jet's sweeping motion.

Flow was illuminated by a pulsed Quantel® Evergreen 200mJ Nd:YAG laser triggered at a specified time interval (15 μ s). The beam is focused using a combination of spherical lenses, and the laser sheet is created as the beam passes through a cylindrical lens. The field of view for the measurement covers a sufficient area, as to image up to 236 mm of the impingement span (note the copper impingement plate is 300 mm in diameter). The laser sheet is on the oscillator centerline, in the plane of jet sweeping flow. Flow was seeded using a Laskin type TSI® oil droplet generator. Seed particles were fed into the plenum upstream of the fluidic oscillator. Mean particle size was approximately 1 μ m, with a typical particle image density of \sim 10 particles per interrogation region. The PIV test cases shown here consists of 1,900 ensemble averaged instantaneous image pairs in order to adequately estimate the mean statistics of interest. Statistical convergence for mean quantities is achieved with \sim 100 image pairs. Images were acquired at a rate of 15 Hz and processed using LaVision's DaVis 8 software. An Andor Zyla 5.5 megapixel (2560 x 2160 pixels) CMOS camera, equipped with a 35 mm focal length lens, was used for image acquisition. A more robust cross-correlation can be achieved by increasing particle image contrast; this was realized by pre-processing all images with sliding background method within DaVis 8. Velocity correlations were then made using a multipass algorithm with an initial window size of 48 x 48 pixels, followed by 4 passes of the "Auto Shape" interrogation window (implemented within DaVis) with a size of 24x24 with a 75% window overlap. Spurious vectors are minimized by using the universal outlier detection scheme implemented with DaVis 8; this is an extra post-processing step after vector calculation. Resulting spatial resolution of the velocity field is approximately 0.74 mm x 0.74 mm. No post-processing filters or vector interpolation techniques were used.

3.1.2 Hot-Wire Background and Description

Hot wire anemometry (HWA) was mainly utilized to study the flow at the exit of the jet on a pulsating flow. This is a method to study turbulent air flow by quantifying the convective heat transfer on a heated wire. HWA measures the mean and fluctuating velocities in the flow. The heat transfer from a heated wire positioned in the fluid depends on the fluid properties (density, ρ , viscosity, μ , specific heat, c_p , and thermal conductivity, k) and the flow properties (fluid temperature, T_{amb} , pressure, P , etc.). The fluid properties are taken at film temperature which is an average of ambient temperature, T_{amb} and wire temperature, T_w .

The heat transfer of a hot-wire probe is an energy balance conducted on an infinitely long wire, where a small section of the wire is shown in Figure 3.1 similar to Bruun [6].

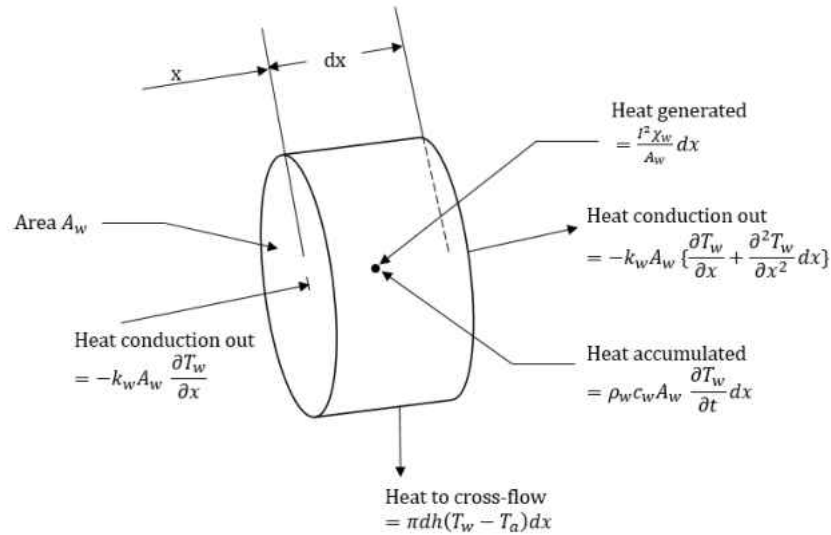


Figure 3.1: Energy Balance of a Small Element

The hot-wire energy balance is shown in Equation 3.1 also given by Bruun [6]:

$$d\dot{Q}_e = d\dot{Q}_{fc} + d\dot{Q}_c + d\dot{Q}_r + d\dot{Q}_s \quad (3.1)$$

Where $d\dot{Q}_e$ is the electrical heat-generation rate, $d\dot{Q}_{fc}$ is the forced convective heat-transfer rate, $d\dot{Q}_c$ is the conductive heat transfer rate, $d\dot{Q}_r$ is the radiation heat transfer rate, and $d\dot{Q}_s$ is the heat storage rate. The electrical heat generation rate is given by the rate of an electrical current, I . For these temperatures, radiation heat transfer rate is, hence, minimal and can be omitted. This equation results in Equation 3.2.

$$k_w A_w \frac{d^2 T_w}{dx^2} + \frac{I^2 \chi_w}{A_w} - \pi dh(T_w - T_{amb}) - \rho_w c_w A_w \frac{\partial T_w}{\partial t} = 0 \quad (3.2)$$

Under steady state conditions, $\partial T_w / \partial t = 0$. This is narrowed down further to where certain terms are considered negligible and the remaining considerable term is the forced convective heat transfer rate. This is then related to an infinitely long wire heat transfer that assumes the conductive end losses may be ignored. A heat balance on a wire segment of length l relates the power input and the convective term shown in Equation 3.3.

$$I^2 R_{w,\infty} = \pi dh l (T_{w,\infty} - T_{amb}) = \pi l k (T_{w,\infty} - T_{amb}) Nu \quad (3.3)$$

Re-writing the equation for hot wire anemometer applications turns to Equation 3.4.

$$\frac{I^2 R_{w,\infty}}{R_{w,\infty} - R_{amb}} = A + BU^n \quad (3.4)$$

Where R_w is the resistance of the hot wire element and R_a is the resistance of the wire at ambient temperature, T_{amb} . The response equation is expressed in terms of the resistance of a Wheatstone bridge components as shown in Figure 3.2. Equation 3.4 is written to consider a balanced anemometer bridge in Equation 3.5.

$$\frac{E^2 R_w}{(R_1 + R_L + R_w)^2} = (A + BU^n)(T_w - T_{amb}) \quad (3.5)$$

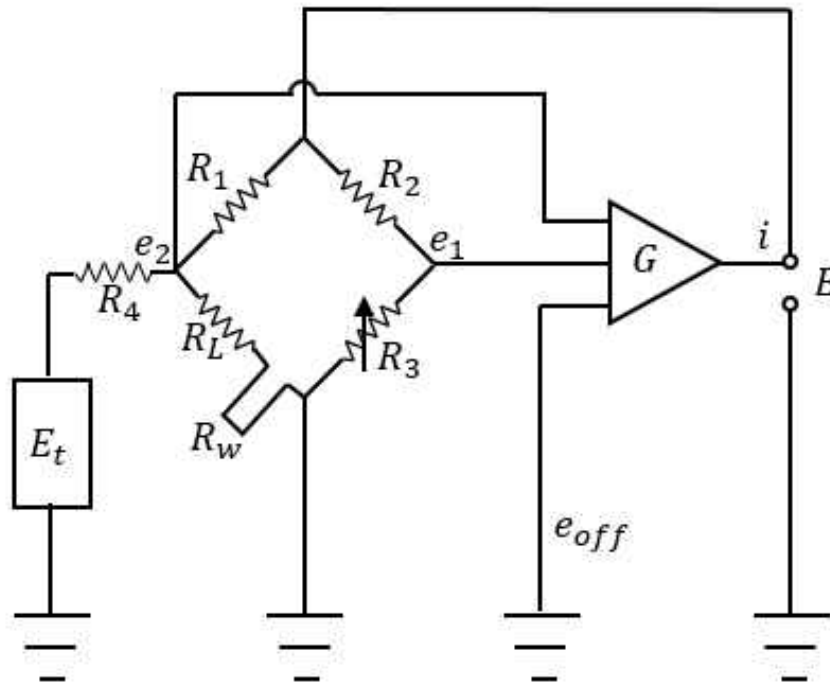


Figure 3.2: Wheatstone Bridge for a Constant Temperature Anemometer

Where R_1 is shown in Figure 3.2 as part of the Wheatstone bridge circuit and R_L is the probe lead and cable resistances. In the case of this project, the resistances necessary to complete the circuit are automatically calculated at the beginning of each test by the Dantec system. For a constant temperature anemometer, the hot resistance R_w remains constant and is independent of the flow conditions. The variables A,B, and n in Equation 3.5 are constant values that are independent of the velocity and the temperature.

A single probe used for this experimental data consists of a miniature wire probe with a diameter of $5 \mu\text{m}$ wire of 1.25 mm length with a long plated tungsten wire sensors. The wire is welded directly to the prongs and the entire wire length acts as a sensor. The probe body is a 1.9 mm diameter ceramic tube, set with gold-plated connector pins that connect to the probe supports by a plug-and-socket arrangement. An overheat ratio of 0.8 was utilized for maintaining the wire

velocity sensitivity. The hot wire-calibration produced a maximum of 2% error for the fluctuating velocity component. The sampling frequency, number of samples, and sampling time was 250kHz, 2,500,000 points for 10 seconds, respectively.

3.2 Heat Transfer Experiments

The heat transfer rig was utilized with the fluidic oscillator as well as the pulsating mechanism. Most of the design was adapted to replace or use the plenum without any alterations to the rig. The basis of rig operation is based on a single jet impinging onto an insulated copper geometry which provides a constant heat flux via a thin heater. The flow originates from an air compressor and passes through 2 redundant flow metering devices: a sonic nozzle and a volumetric flow meter by OMEGA. From this point onwards the flow path and various instrumentations can be seen within the experimental testing in Figure 3.3.

From this point, the flow then enters a plenum where it experiences several means of flow conditioning. The compressed air lines are connected into the plenum and immediately impinge on a "splash plate", which slows the flow significantly and helps provide a more uniform flow profile through the plenum. Additionally, one flow straightener plate is located within the plenum, originally for providing a more uniform flow, for structural support purposes in holding and aligning the motor.

The blue stair steps seen in dark blue on the top of the acrylic rig top lid is a machined piece to set the height between the copper surface and the impinging jet orifice, also known as z/d metric which represents the jet-to-target surface spacing. This works in conjunction with the plenum being bolted onto an aluminum plate, which is constrained to only translate in the direction normal the copper test article surface (via the metal rods sticking up from the acrylic top lid in Figure 3.4). This connection between the plenum and the acrylic top lid allows for a handle to be spun to enable translation (changing of z/d) of the plenum in the vertical direction.

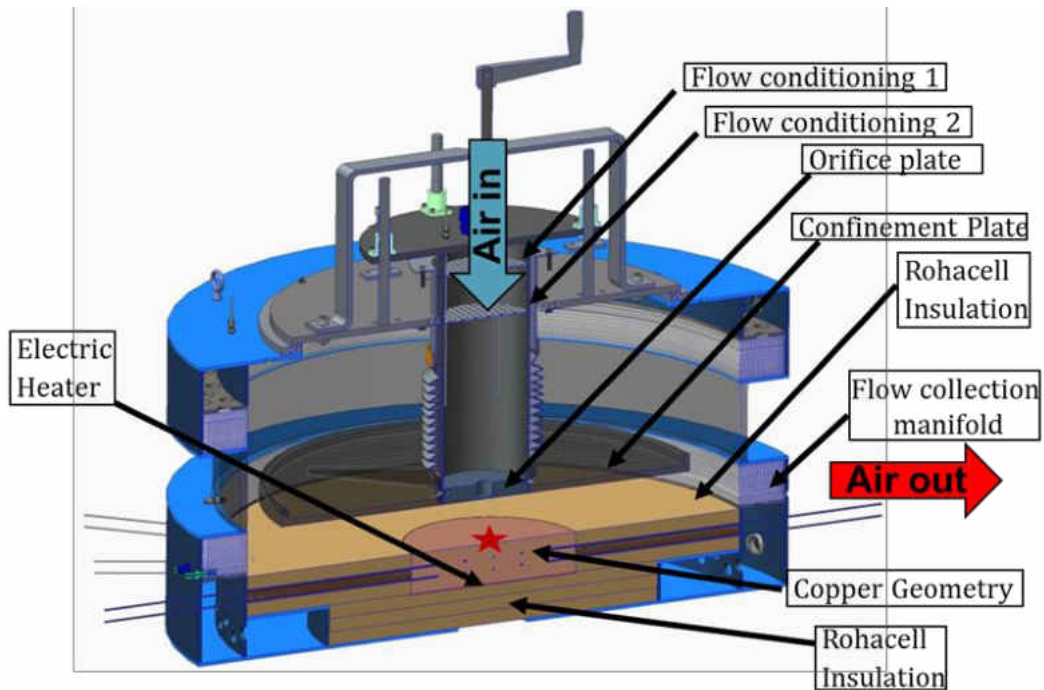


Figure 3.3: Isometric View of Heat Transfer Rig

Once the air passes through the plenum it then exits through the orifice plate, creating the impinging jet which develops in the rig environment until impinging on the target copper surface. This orifice is a sharp edge orifice, with a thickness to jet ratio of unity ($L/d=1$). The orifice plate is bolted to remain within, and concentric to, the plenum. The plenum is an acrylic cylinder which is mounted to the aluminum rig body as pictured in recent figures as well as discussed in brief.

The impingement air jet developments from the sharp edge orifice plate until stagnating on the copper test article surface. The impinging jet is influenced by the surrounding flow field, which is confined by the confinement plate, as pictured in Figure 3.3. The confinement plate is much larger than the copper surface where the heat transfer measurements are made. The confinement plate approaches the outer perimeter of the metal casing of the rig walls. In this gap between the confinement plate and the outer rig walls, an additional air jet is introduced. This air jet is called the pressurization flow jet. This air jet enters the rig in the upper portion, and passes through this

cavity between the confinement plate and the rig side walls. The purpose of this pressurization jet is to provide a stable and repeatable recirculation in the impinging jet environment through the series of z/d heights, Reynolds numbers, surface geometries, etc. Otherwise, for example, a change in the jet-to-target surface spacing could provide a unique change to entrainment of the impinging jet, and thus differing jet temperatures at the copper surface. This pressurization flow jet was studied at the time of its inception to the rig through a series of entrainment tests, to ensure accurate results were achieved for jet temperature during heat transfer testing.

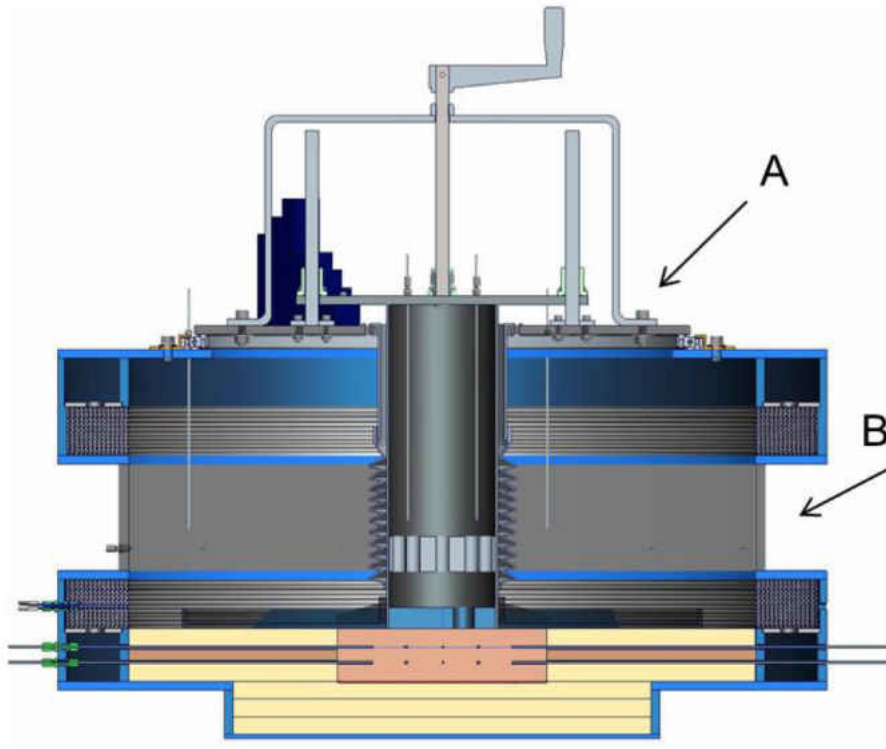


Figure 3.4: Section Cut View of the Rig Where the Top Acrylic Lid (A) and Side Chamber Walls (B)

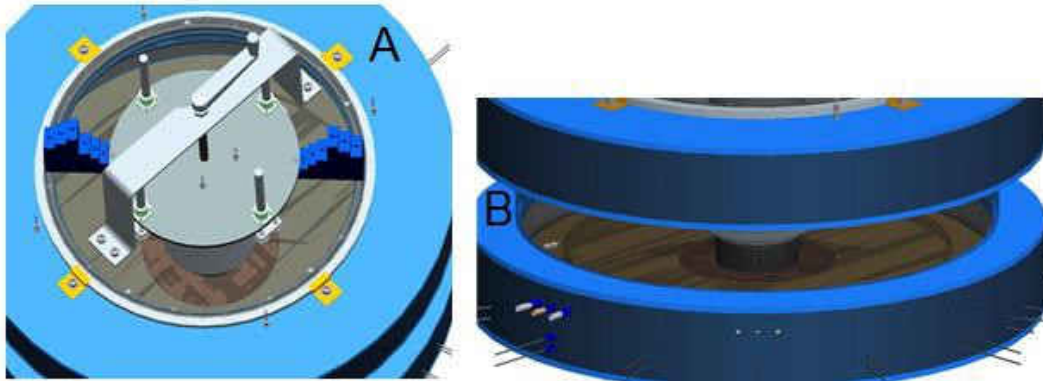


Figure 3.5: Alternative Views to the Acrylic Top Lid and the Chamber Side walls from Figure 3.4

After the impinging jet stagnates onto the copper test surface, the flow forms a wall jet and the fluid moves parallel to the copper surface until it reaches the exit of the rig. This exit area is comprised of a series of screens, termed the flow collection manifold in Figure 3.3. From here, the flow collects in an annulus uniformly, and is routed to several uniformly spaced exits (circular tubes plumbing from the rig to the discharge into laboratory ambient environment).

Now that the flow path has been described in some detail, the details pertaining to the rig's heating will be discussed. The heat is provided to the copper geometry through a thin silicone-rubber heater (manufactured by OMEGA), which is controlled by a VariAC transformer. This magnitude of power provided to the heater is such that a 30 °C differential in temperature between the jet and the copper surface is maintained. This is on the order of 300 – 800 Watts (in general).

3.2.1 Temperature Measurements

Several temperature measurements are acquired during data acquisition and testing of this rig. A number of temperatures are taken throughout the rig to ensure adequate measurements of the flow temperatures are being acquired, and to also especially ensure accurate measurement of the copper test articles during testing. For the thermocouples used in this rig and testing of such, T

type thermocouples (TCs) are used which have been calibrated at the Siemens Casselberry facility. The range of temperature measurements reside between approximately 20°C - 70°C. Two types of thermocouples (TC) are used within this rig; the traditional laboratory TCs with very thin electrical wire which combine to a single bead, and also long sheathed TCs which are rigid and have electric terminal plugs at one end for connection to the TC extension wire. The first kind of TCs are used for flow measurements within the rig, where the second type (long rigid metal rods) is used for temperature measurements within the copper test articles and also the air temperature as the flow exits the rig. The location, quantity, and purpose of both of these will be described in detail in the following section in detail.

The second kind of TCs mentioned are 24” long, grounded, 0.125” diameter instruments from TC Direct Corporation. These long metal cylinders are rigid and inserted into the rig with a tight fit to the aluminum casing (utilizing a grommet). The location and quantity of the TCs installed, for traditional heat transfer testing done to acquire correlation data, and used for data acquisition can be seen below in Figure 3.6. It should be noted that many other mini investigations were conducted with additional TCs installed, for example one which investigated recirculation air temperatures for varying test conditions, and as such will not be included in this list for sake of conciseness.

As mentioned above, the surface temperature of the copper test articles was acquired based on an extrapolation of the TCs interior to the copper test article itself. This will be expanded upon here, as it is a crucial detail in the determination of accurate area averaged heat transfer coefficient characterizations for copper block style testing. In general the area averaged heat transfer coefficient is calculated using an energy balance on the copper block surface. This energy balance requires knowledge of the target (copper) surface temperature, and jet temperature (i.e. $\Delta T = T_{surface} - T_{jet}$). To acquire the surface temperature values, several TC measurements within the copper geometry are considered and linearly extrapolated to approximate the surface temperature.

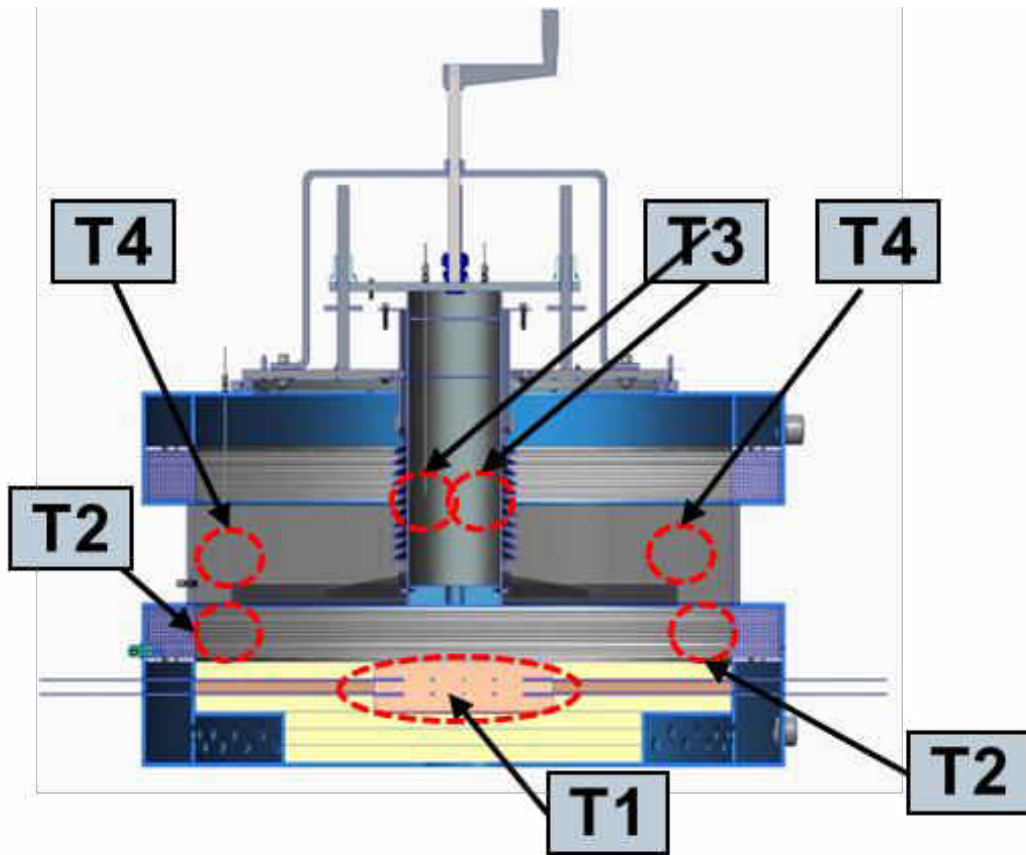


Figure 3.6: Temperature Measurements Within the Rig

Sixteen TCs are placed within a single plane within the copper at one height (synonymous with saying at one thickness, row, or z/d location), and 16 additional TCs are placed at in a separate plane at one additional copper height location. This can be seen in Figure 3.6, where sample TC locations are visualized as dots in the “Section B” and “Section A” diagrams. Each section represents a planar section within the copper test article, consisting of 16 TCs. These two planes are at different displacements from the heat transfer surface, and are used to extrapolate an approximated surface temperature.

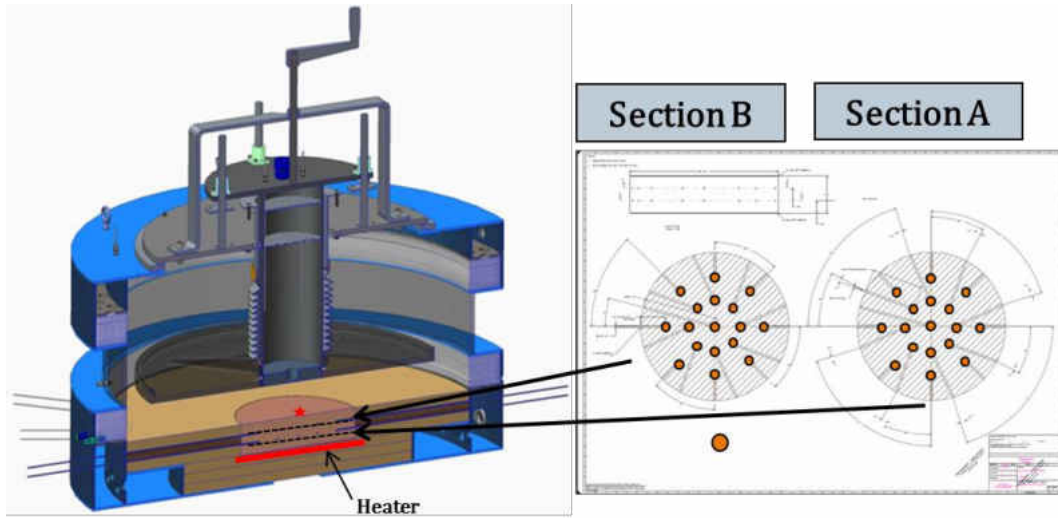


Figure 3.7: Sample Measurement Planes Section A and B for the TCs Within the Copper Test Articles

As discussed, the baseline geometry was tested with intrinsic TCs, with a means to compare the extrapolated approximations of surface temperature to these intrinsic TC measurements. These intrinsic TCs were tested in a scientific grade temperature oven prior to installation, to ensure they were accurately capturing the temperature, for a temperature range within that of the experimental test rig. 40 flat plate (baseline) tests were conducted, and the results demonstrate good agreement between the surface intrinsic TCs and the extrapolated surface temperature approximation. The results show a maximum deviation between the two temperatures to be $0.53\text{ }^{\circ}\text{C}$, with an average deviation of $0.43\text{ }^{\circ}\text{C}$. Bearing in mind the uncertainty in TC measurements being $0.5\text{ }^{\circ}\text{C}$, this is an acceptable deviation. As shown in Figure 3.7, sample measurement planes, displayed as section A and B, are embedded with TCs within the copper test article. Each section is averaged to gather a single value of temperature at a single location. The two respective planes are used to extrapolate an approximate surface temperature of the copper test articles.

3.2.2 Mass Flow Measurements

The experimental testing rig utilized two flow rate measurement devices for the sake of redundancy and accuracy in measuring the flow rate of the impinging jet. This mass flow rate is used to generate the corresponding Reynolds number by Equation 3.6. The equation is converted to consider the mass flow rate instead of a measured velocity for Reynolds number.

$$Re = \frac{\bar{U}d}{\nu} = \frac{\dot{m}d}{\rho A \nu} = \frac{4\dot{m}}{\rho \nu \pi d} = \frac{4\dot{m}}{\mu \pi d} \quad (3.6)$$

The first method of measuring the flow rate of the impinging jet utilized one of two volumetric flow meters (make: OMEGA, model: FMA-1613A and FMA-1622A), used depending on the testing condition and mass flow rate required. These devices measured the volumetric flow rate of the impinging jet (flow through the plenum), and with corresponding temperature and pressure measurements a mass flow rate was thereby calculated. The devices were located about 2 meters upstream of the plenum entrance.

The second device which was used to measure the impinging air jet flow was a sonic nozzle, typically used to calibrate other flow measuring devices (e.g. venturi's) due to its highly accurate flow measurements (Model: SN-32-AN-0.177-SS, Throat Diameter: 0.177"). This device was located far upstream (~9 meters upstream of the plenum), very close to the location of the air compressed line which provides the compressed air from the large compression tank. Due to this device's accuracy, flow meters up stream of the plenum were utilized in the definition of Reynolds number per each testing case.

3.2.3 Heat Leakage

In order to correctly quantify the heat swept from the copper surface due to the impinging jet, the heat lost through the copper backside conduction must be quantified. This is done through a series of small test investigations. These heat leakage tests are conducted in a research laboratory

setting, involving stuffing the rig cavity with insulation and measuring the required heat input to maintain a steady copper temperature. The net heat addition from the copper is determined from correlations of temperature versus power. Three copper temperatures are selected spanning through all copper temperatures when testing. The voltage supplied to the copper block and the room temperature are recorded. Said measured heat input to the rig corresponds to the heat leaving the rig environment through copper backside conduction.

3.2.4 Addition of Fluidic Oscillator

The parameters of the current heat transfer rig were provided to FDX Fluid Dynamix GmbH (subsequently denoted as FDX) for exploring the current innovation of fluidic oscillators as a collaboration with Siemens Corporation. FDX is known for developing and producing OsciJet nozzles and other fluidic devices. In case of this cooperation a proof of concept, the oscillator was designed to also optimize for the internal blade cooling in order to determine possible efficiency gains through sweeping jets. The design was focused in the rig's constraints. With that being said, the oscillator replaced the prior plenum and was bolt down to the confinement plate, when necessary. The flow entered a smaller plenum with height of 15 cm where the splash plate and a flow straightener plate would break down any large vortices and straighten the flow before entering into a contracting nozzle part of the fluidic oscillator. The confinement plate would be removed for cases of understanding the effects of entrainment allowing the flow to move upwards in the cavity.

To properly compare the steady jet and fluidic oscillator jet, the hydraulic diameter was kept constant and the same shape of square. Generally, a square jet differs from a circular jet due to the counter-rotating vortices formed at the corners. A look into the heat transfer results of a circular and square jet determined a significant difference that may have been biased for comparison purposes.

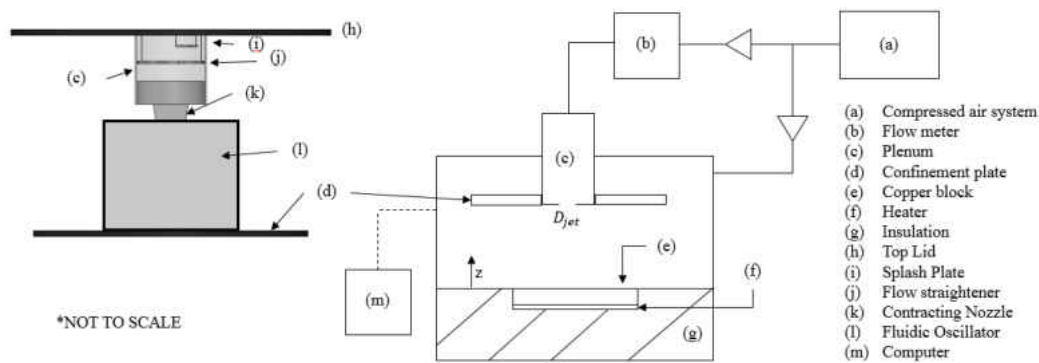


Figure 3.8: Fluidic Oscillator Setup

3.2.5 Addition of Pulsing Mechanism

An intensive understanding of all the components needed to take into account when adding a pulsing mechanism required much consideration. Figure 3.9 describes all the components considered for the pulsing mechanism. The addition of the components were all located within the plenum of the heat transfer rig. The original components within the plenum stayed the same with their functions having a different purpose. That is, the flow straightener was mainly used for structural reasons rather than straightening the flow. The rotating disk that generated a pulsing jet was placed within the orifice plate at the bottom of the plenum. A motor and its mounts were added inside the plenum. All the pulsed cases considered a confinement plate as shown in Figure 3.9.

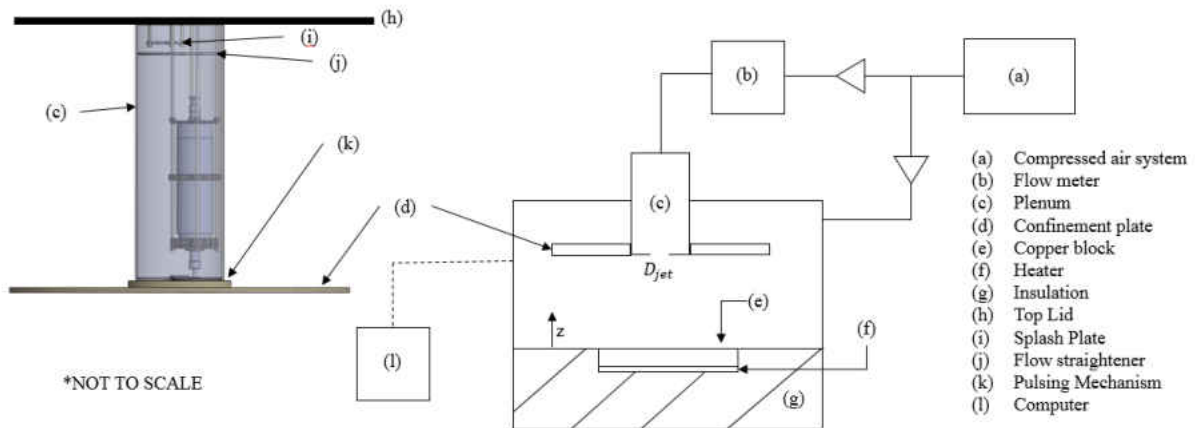


Figure 3.9: Pulsed Setup

Figure 3.10 demonstrates the components within the plenum and orifice plate assemblies. The flow would enter through one hole at the top of the plenum impinging on to a splash plate to disperse the flow. A flow straightener with 7 mm diameter hole sizes was placed around 8 cm below the splash plate which was mostly used for structural purposes. Four rods were bolted from the top of the lid to the flow straightener. Then, three long threaded rods would bolt the flow straightener to the motor through a series of three mounts. The motor was a 65 mm spindle motor typically used for CNC engraving machines. Balancing the motor to keep the disk in the correct location within the plenum proved to be time-consuming and difficult since the tolerances within the orifice plate were adjusted to block flow from leaking through the cavity of orifice plate rather than the jet hole seen in Figure 3.10. The mounts were 3-D printed and placed on the top, center, and bottom of the motor. The bottom mount had levels to assist with balancing the motor. A custom-made shaft was placed at the end of the motor where the collet of the motor would grasp the unthreaded portion and the disk would be placed on the threaded portion. A flange on the shaft was used to hold the disk in place and for balancing the disk properly. A nut was screwed below the disk to keep the disk in place. Two 3-D printed lips were placed at the entrance of the jet and below the disk to permit flow from leaking into the cavity of the disk. The tolerances above and

below the disk cavity within the orifice plate was 3 mm each.

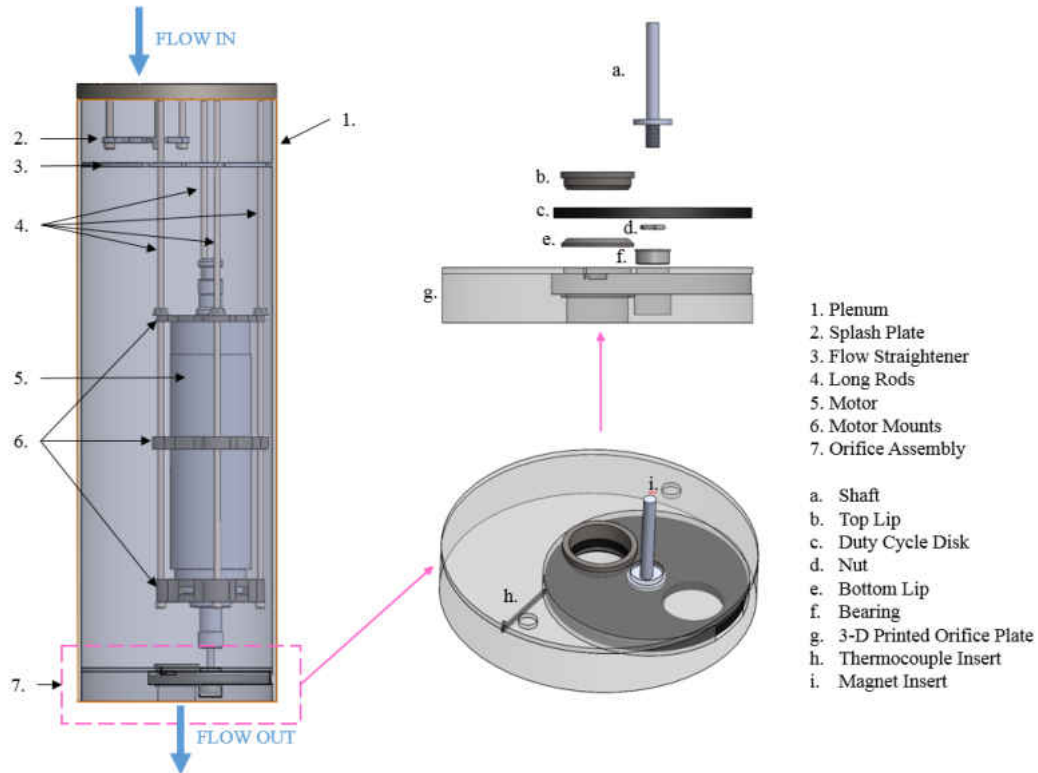


Figure 3.10: Pulsed Setup - Plenum and Articles

The orifice plate was printed as two separate sections to facilitate in removing the disk. These two sections of the orifice plate stuck together using two magnets 180° from one another referenced as (i) in Figure 3.10. This was done to confine the disk and prevent the jet to be influenced by any flow effects that may occur above a rotating disk. The duty cycle disk was exchanged by removing the bottom section of the orifice plate and loosening the nut on the shaft. A self-aligning flanged ball bearing, referenced as (f), was placed below in another cavity within the orifice plate to assist the shaft with alignment. A TC was placed within the insert of the orifice plate to consider the temperature of the orifice plate, referenced as (h). Due to friction between the lips and the disk, the orifice plate heated up and may have affected the jet temperature slightly but

was taken into account. The confinement plate was bolted to the plenum and the orifice plate and flush to the exit of the jet.

To vary the duty cycle, several disks were printed and placed on the shaft that would close and open the jet hole as seen in Figure 3.11. The final result was testing 3 duty cycles for 6 frequencies each. To vary the motor's frequency, a variable-frequency drive (VFD) would enable the motor to spin between 0 - 400Hz. This frequency, however, did not correspond to the flow's frequency. All three duty cycle disks contained two holes 180° from one another. Thus, the jet's frequency was considered twice the VFD's frequency. In other words, a frequency reading of 400 Hz on the VFD would denote a jet's frequency of 800 Hz. In the current text matrix the lowest and highest frequency tested was 20 Hz and 400 Hz, respectively.



Figure 3.11: DC Disks: 27% (left), 33%(center), and 50% (right)

The definition of duty cycle varies from author to author as the pattern on the disk varies. The duty cycle, DC, definition used in this work is considered as on area over total area as written in Equation 3.7. The constant 2 in the numerator signifies the amount of holes in the disk.

$$DC = \frac{OnArea}{TotalArea} = \frac{2\pi r_{jet}^2}{\pi[r_{out}^2 - (r_{out} - 2r_{jet})^2]} \quad (3.7)$$

Where r_{jet} is the radius of the open hole and r_{out} is the radius of the disk. Once the holes were extended seeming to look kidney shaped, the equation was adapted to consider half circles and the selected angle the holes were extended until. The duty cycles were selected based on the

available working area on the disk as well as to prevent major fluctuations from the disk.

3.3 Uncertainty

The measurement error is quantified for the measured heat transfer and flow tests that considers a methodical approach of reaching the true values. The measurement error considers the random error as well as the systematic error, [3]. The random error, known as precision, is taken into account by repeating the same test to characterize the random error observed from the equipment. This is observed in this project by repeating the same test 5 times at various time and dates. The systematic error, known as bias, is a fixed quantity that is not as random as precision errors. With practical experiments, a small sample is considered; thus, a student's t-statistics table is characterized by the degrees of freedom and confidence interval. With that being said, the degree of freedom in these tests is 4 and a confidence interval of 95% is selected as it is standard in experimental cases. The uncertainty of the frequency of the pulsing mechanism, not displayed in the table, obtained from the VFD was +/- 3 Hz.

Table 3.2: Uncertainty

Quantity	Mean Value	+/-	Confidence Interval
Nusselt Number	80.35	6.89	95%
Reynolds Number	30,033	867.8	95%
Average Velocity (m/s)	30.59	2.89	95%

The results are shown in Table 3.2. The uncertainty tree for the Reynolds number and Nusselt number is broken down in Figures 3.12 and 3.13, respectively. In terms of the uncertainty in the velocity data, a quantified value is given in the Dantec Dynamics® user guide that is performed on the data.

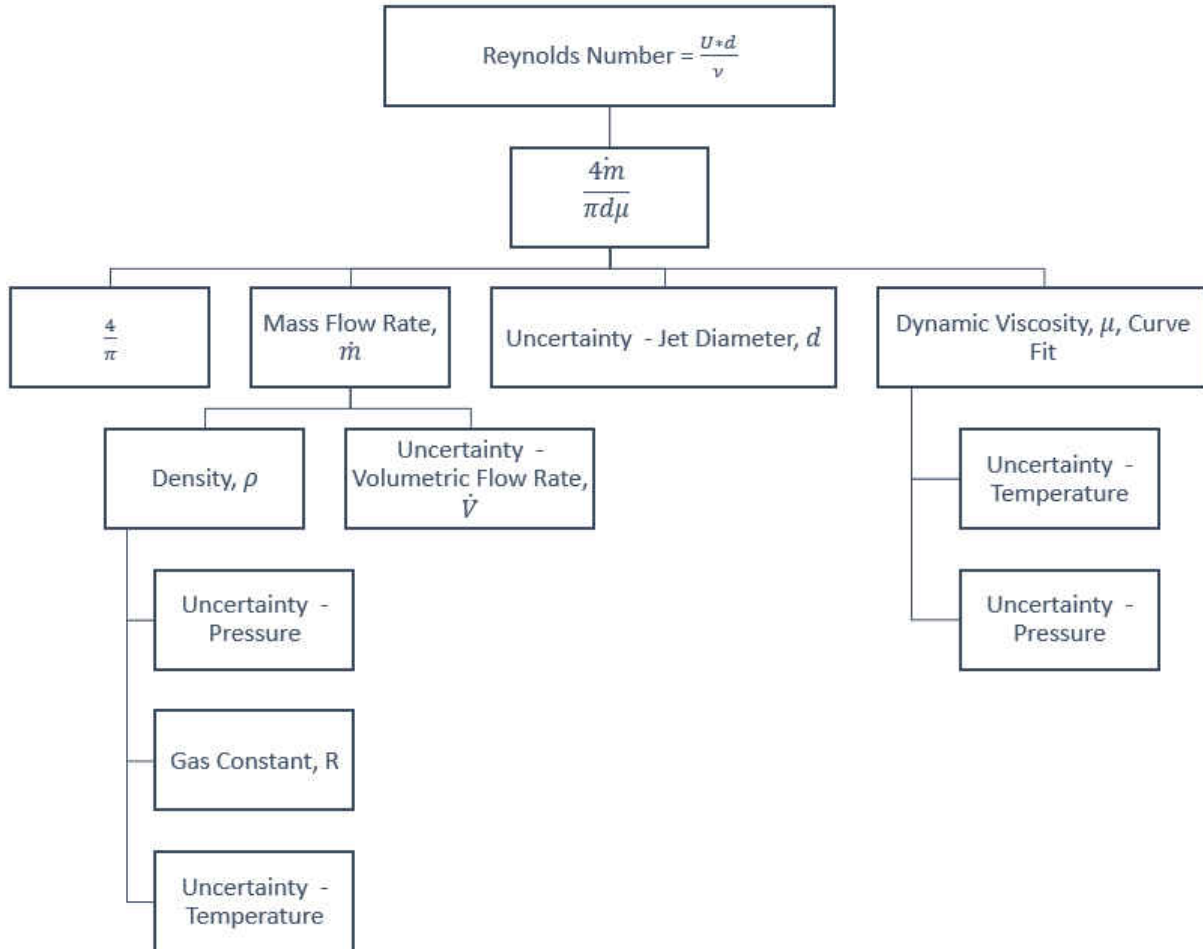


Figure 3.12: Uncertainty Tree - Reynolds Number

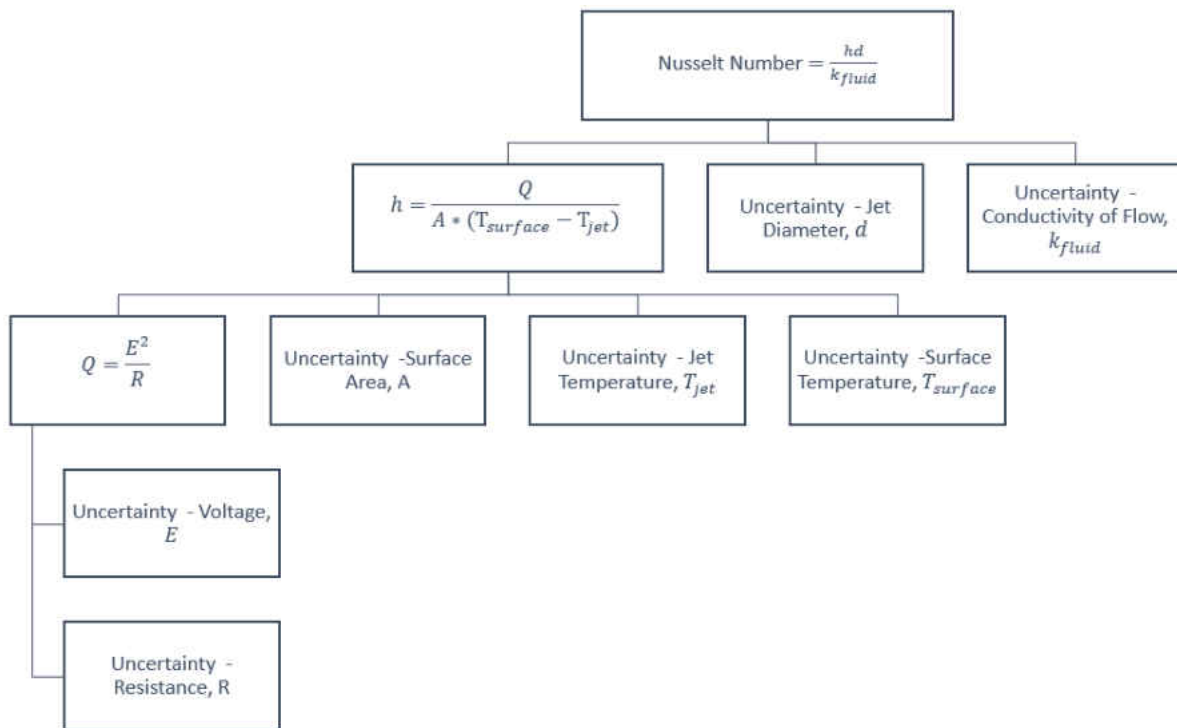


Figure 3.13: Uncertainty Tree - Nusselt Number

CHAPTER 4: ANALYSIS OF FLUIDIC OSCILLATOR

The OsciJet Nozzle is part of the Siemens network that investigates and stimulates innovations with the corporation -in this case in particular for the Siemens Power and Gas division. The FDX Fluid Dynamix GmbH (subsequently known as FDX) develops and produces OsciJet nozzles and other fluidic devices. In case of this cooperation a proof of concept was conducted regarding the optimization of an OsciJet Nozzle for the internal turbine blade cooling in order to establish potential efficiency gains through a sweeping jet.

Nozzles are stationary devices that create a sweeping jet that is a self-sustaining flow which is unstable inside of the device. With their in-house technology platform, FDX is able to design these devices with respect to the space-envelope, jet characteristics, pressure loss, frequency, and spray angle. The spatial distribution of cooling air is enhanced as well as the degree of mixing through turbulence is advanced by the fluidic oscillator, which would increase the cooling efficiency. These considerations are presented in Table 4.1 where the proposed values were given to the manufacture and the actual values were measured based on the PIV results.

Table 4.1: Fluidic Oscillator Design Parameters

Fluidic Oscillator Design Parameters		
	Proposed	Actual
Pressure Loss (psi)	0.032	0.024
Pressure Loss (Pa)	216	165
Sweeping Frequency (Hz)	4.53	5.49
Sweeping Angle (°)	~63	36

4.1 Flow Analysis Results

The testing matrix for the oscillator is given in Table 4.2. The flow analysis considered the mean velocity fields, boundary layer for a confined case, and the Reynolds stresses for a confined case. Due to some of the results being quite similar between the unconfined and confined case, the data presented would represent both scenarios unless stated. Things to note about the data from the oscillator: the term z/d is the spacing between the jet exit to the surface which is non-dimensionalized using the jet diameter; the term r/d is the radial location on the surface which is non-dimensionalized using the jet diameter; the fluidic oscillator is denoted as FO and baseline as B sometimes; and both oscillator and baseline have the same square hydraulic diameter exit.

Table 4.2: Fluidic Oscillator Flow Analysis Matrix

Fluidic Oscillator Heat Transfer Testing Matrix				
Jet Case	Reynolds Number	z/d	Jet Diameter, d (mm)	Other Parameters
B	30,000	2, 3, 4, 6	28	Confined/ Unconfined
FO	30,000	2, 3, 4, 6	28	Confined/Unconfined

4.1.1 PIV Confined/Unconfined Mean Velocity Fields

Figure 4.1 shows the evolution of the symmetrical axial mean velocity versus the radial direction of the jet as it sweeps and impinges on the surface for confined and unconfined cases. The horizontal corresponding to r/d is a non-dimensional term based from the jet diameter. The field images presented depicts then a 24 cm section of the 30 cm copper surface. The radial direction is centered at the stagnation point matching to the the center of the jet.

For all cases, the center line velocity diminishes as the jet mixes with the entraining air before impinging on the surface. Also the deflection zone corresponding to the area above the stagnation point exhibits the same velocity field as a steady jet where there is a decrease in axial velocity [25]. An interesting aspect is seen at z/d of 4 and 6 where the stagnation region is almost

negligible due to the sweeping motion and does not build up a high static pressure region contrary to a steady jet where the highest heat transfer occurs. The two lobes formed from the sweeping jet observed by Agricola [1] starts from z/d of 3 at an $r/d = 1.0$. These lobes move radially outwards as the z/d increases.

No significant information is seen from the flow field of an unconfined case in Figure 4.1 that would add value to the explanation of the heat transfer or the effects of a confined versus unconfined jet. The jet displays the same behavior while possibly attracting more entrained flow. Further comparison of confined versus unconfined will be evident when comparing the Reynolds Stresses and boundary layer profiles.

The velocity profile close to the surface can be seen in greater detail in Figure 4.2 where both cases vary greatly. The horizontal axis, r/d , is the radial location left of the stagnation point. Therefore an $r/d = 0$ is the vertical symmetrical line. The baseline case exhibits the same behavior with varying jet-to-surface spacing, z/d , with the velocity magnitude being the highest at the stagnation point and an abrupt velocity decrease after a non-dimensional radial distance of 1 as expected. Increasing the z/d for the baseline case results in the velocity to decrease by more than 30% in the stagnation region.

The fluidic oscillator velocity profile in Figure 4.2 displays no noticeable trends with variations in z/d . The lowest z/d of 2 has a similar trend as the baseline where the peak is significantly higher at the stagnation point and decreases rapidly after an r/d of 1. For z/d of 3 to 6, the peak at the stagnation region is less noticeable and the flow spreads out radially while approaching a uniform velocity. This is where the two lobes form as seen in Figure 4.2 as the jet's speed significantly decreases. This can explain why the fluidic oscillator performs better at lower jet-to-surface spacings since the stagnation region typically is the main area of heat removal.

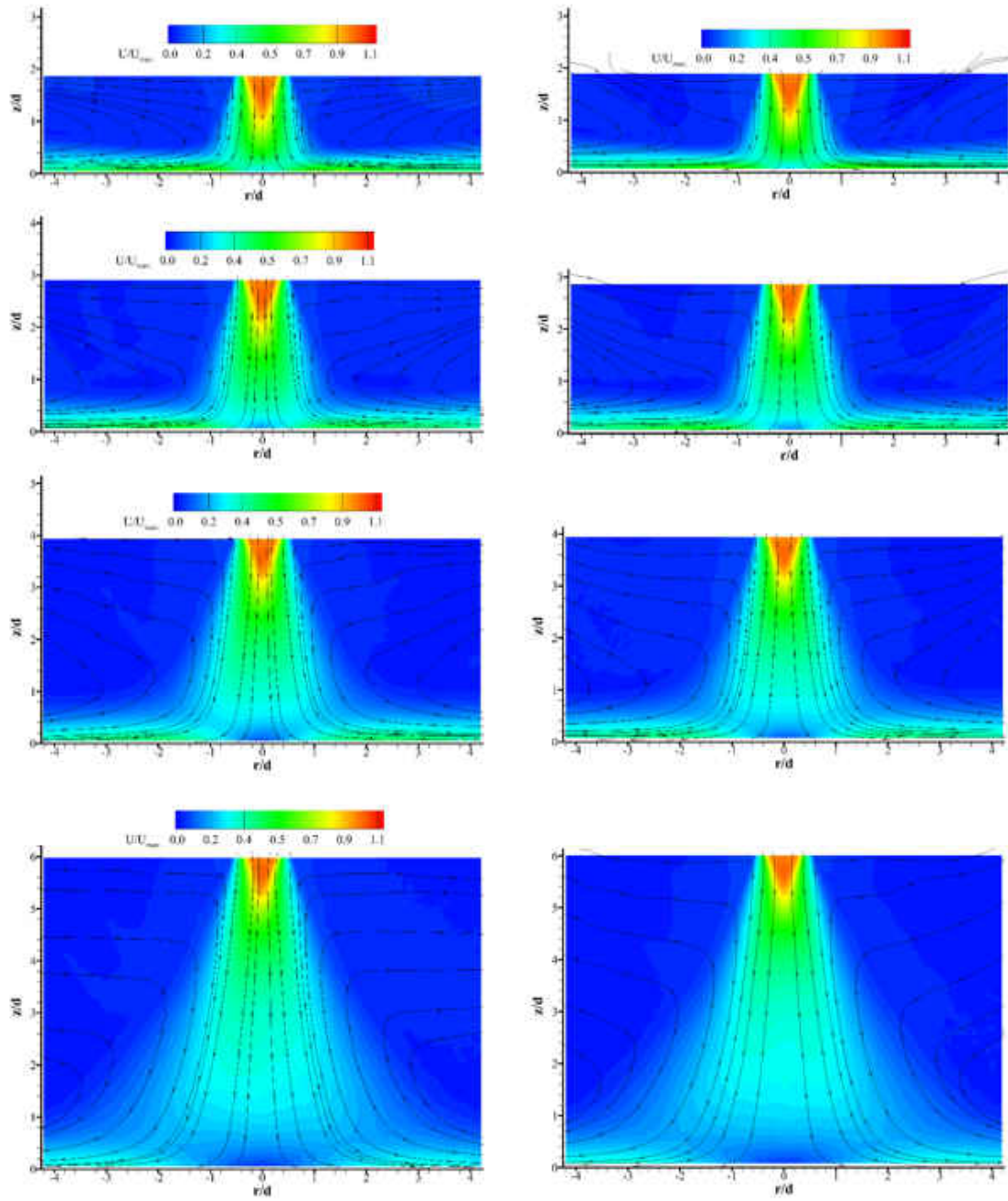


Figure 4.1: Mean Velocity Fields for Different $z/d = 2, 3, 4, 6$ (top to bottom) and Confined (left) and Unconfined (right), Respectively.

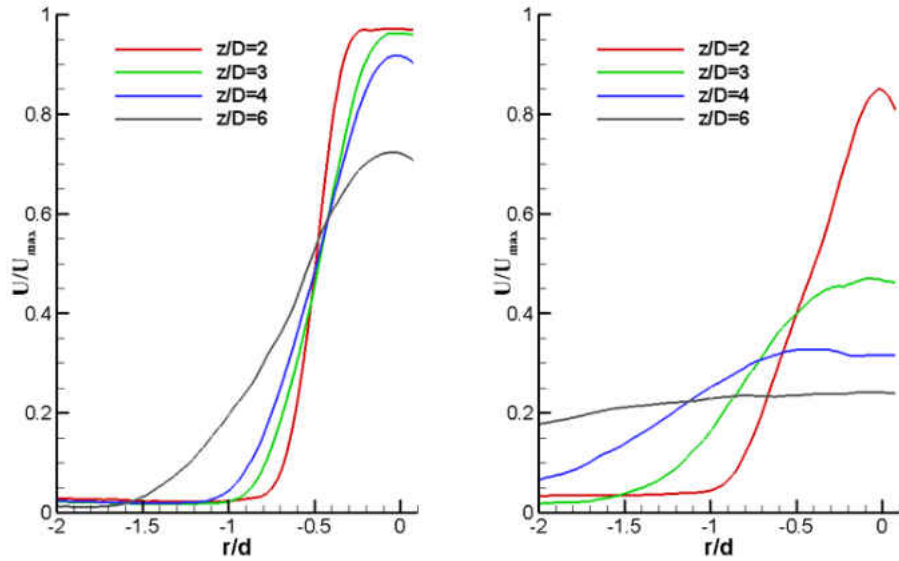


Figure 4.2: Non-Dimensionalized Velocity Plotted at $z/d=1$ for $z/d=2,3,4,6$ for Baseline (left) and Fluidic Oscillator (right)

In addition to the insight provided, Figure 4.3 compares the boundary layer formed post-impingement on the surface of the baseline case and the fluidic oscillator for a confined case. This is done specifically for the lowest z/d of 2 that may correspond to the highest heat transfer removal. The r/d locations relates to the positions in Figure 4.4 as the flow moves further from the stagnation region. The baseline used as reference shows how the boundary layer is diluted the further out it reaches as it mixes with the ambient flow above. However, the FO's boundary layer is consistently denser as the flow moves outward.

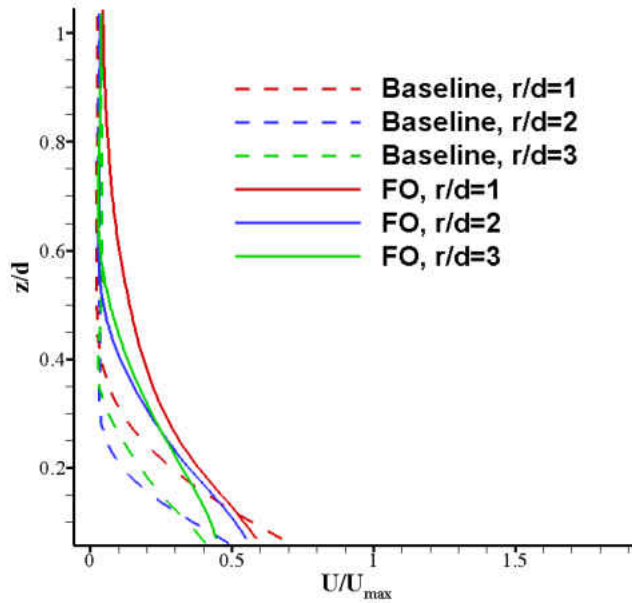


Figure 4.3: Wall Jet Velocity Profiles for Baseline and FO at $z/d=2$

4.1.2 PIV Boundary Layer Confined/Unconfined Comparison

The following boundary layer plots presented in Figure 4.4 associate to different locations and heights as shown in Figure 4.5 for 4 z/d . Starting at $r/d=1$, the $z/d = 2$ has a high speed flow close to the surface and gradually slows down with increasing r/d . At $z/d=6$, it appears the flow at the stagnation area is affecting the boundary layer with the sweeping motion inhibiting the boundary layer to develop. After an $r/d=3$, the flow slows down exhibiting a decrease in thickness due to the entrainment mixing with the boundary layer and is not affected much by the jet-to-surface spacings. This will later correlate to the Reynolds stress component in Figure 4.7. Thus, it can be concluded that the sweeping motion caused by a fluidic oscillator may be beneficial for lower jet-to-surface spacings where the developed boundary layer assists with the heat transfer.

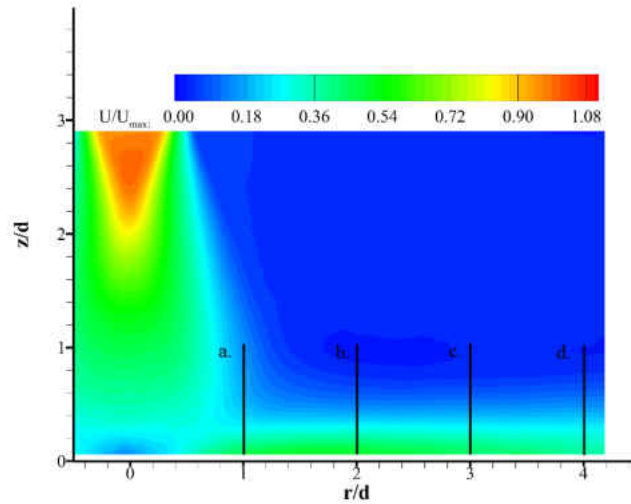


Figure 4.4: Boundary Layer Locations Where (a.) is $r/d = 1$, (b.) is $r/d = 2$, (c.) is $r/d=3$, and (d.) is $r/d=4$

The unconfined boundary layer profile showed the same result as the confined case for a $z/d=2$ and 3 due to the entrainment effects not affecting the boundary layer considerably; thus, a comparison of confined versus unconfined for a z/d of 4 and 6 will be discussed as shown in Figure 4.6, respectively. At a $z/d = 4$ for confined and unconfined, the boundary layer close at an $r/d = 1$ is experiencing slow velocities where the lobe is not present as shown in Figure 4.1. After the boundary layer for an r/d between 2 and 4 forms. The confined tends to have a high momentum flow close to the surface when compared to the unconfined; nonetheless, the confined flow seems to mix more with the entraining flow above the surface and is almost identical to the unconfined boundary layer. At a $z/d=6$ (figure to the right), the lobe is formed past an $r/d= 1$ but the flow slows down at a faster rate compared to $z/d = 4$. The addition of the confined plate does not make much of a difference on the boundary layer to notice for a $z/d = 4$ and 6.

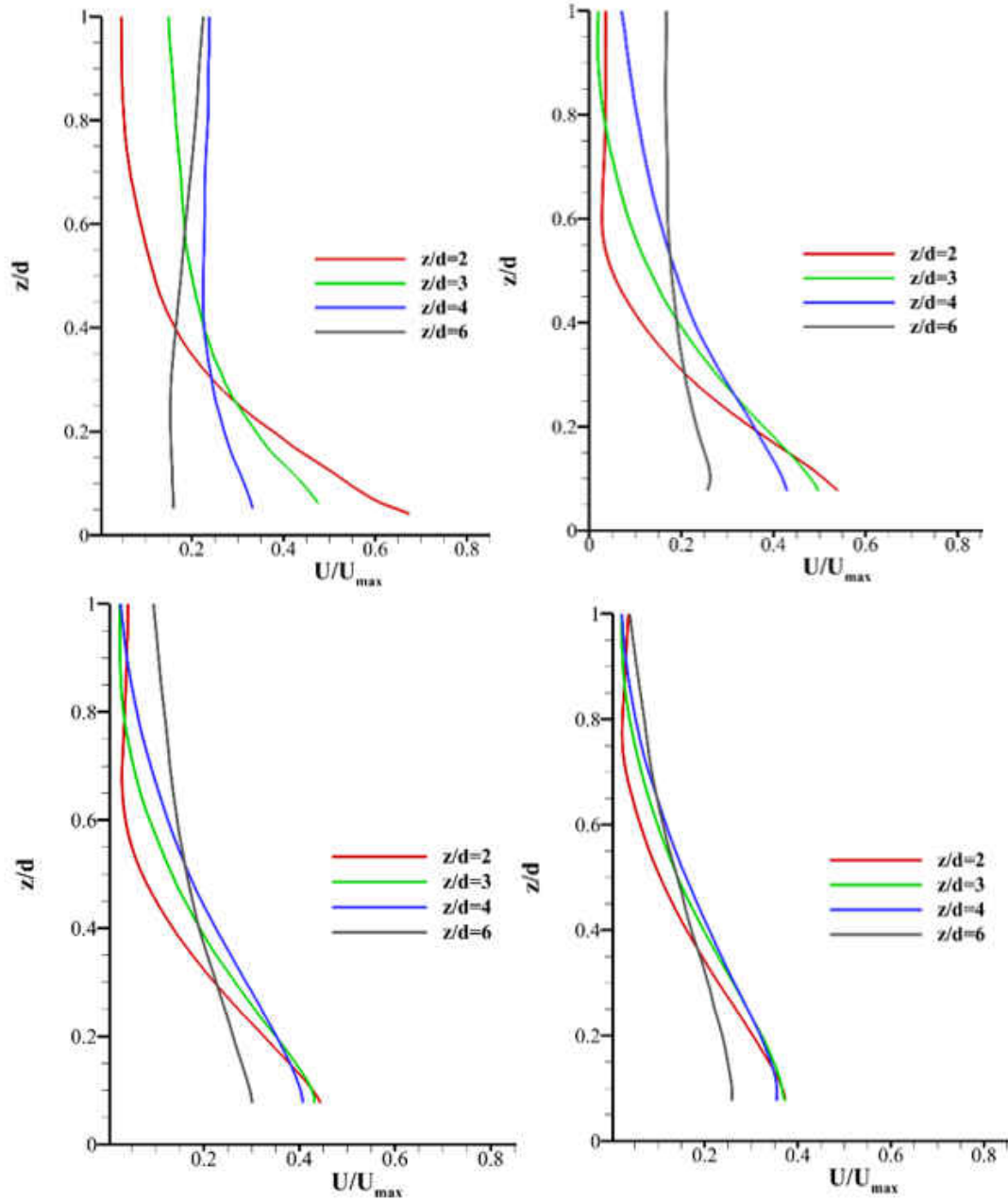


Figure 4.5: Boundary Layer Profile at Various Streamwise Locations for Confined Case, $r/d = 1$ (Top Left), $r/d = 2$ (Top Right), $r/d = 3$ (Bottom Left), $r/d = 4$ (Bottom Right)

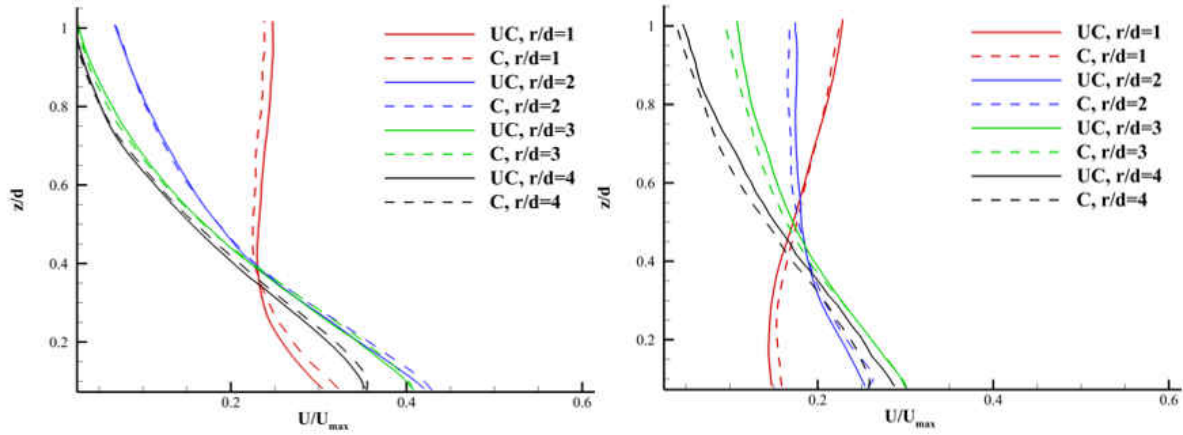


Figure 4.6: Boundary Layer Profiles Comparison for Confined (C) and Unconfined (UC) at Various Radial Locations for $z/d=4$ (Left) and $z/d=6$ (Right)

4.1.3 PIV Confined Reynolds Stresses

The turbulence terms in the conservation of mass equation for incompressible flows can be interpreted as a stress on an element of the fluid in addition to the stresses determined by the pressure, P , and the viscous stresses [18]. The Reynolds Stresses provide insight on regions experiencing high levels of mixing, presented in Figure 4.7. The Reynolds stress scale in the baseline case varies ± 2.5 while the sweeping jet changes ± 25 validating the increase in mixing for a sweeping jet in the domain. The typical boundary layer growth of a steady jet is noticed in all figures while the sweeping jet develops a boundary layer only at the lower z/d spacings. The jet core of the baseline case reaches the surface at low z/d . There is a high level of turbulence in the boundary layer up to a z/d of 4. At a z/d of 6, there are local spots of high mixing but the jet core is dissolved by the entraining flow; nonetheless, the boundary layer is still formed due to the jet for all images in the baseline cases. Generally the location of mixing for the baseline case occurs in the same region. The fluidic oscillator's jet core interacts greatly with the surface and forms local turbulence at the z/d of 2 and 3. For a z/d of 4 and 6, however, the sweeping motion prohibits the high levels of turbulence close to the surface. Stagnant air forms above the stagnation

region affecting the heat transfer in this location. The length of main turbulence remains to be a $z/d = 2$ (red area) while anything after that is mixed with the entrainment flow. To tie it up with the boundary layer, a general conclusion can be understood about the oscillator. In order for the oscillator to perform better than a steady jet, a dense boundary layer with high levels of mixing is what improves the heat transfer performance.

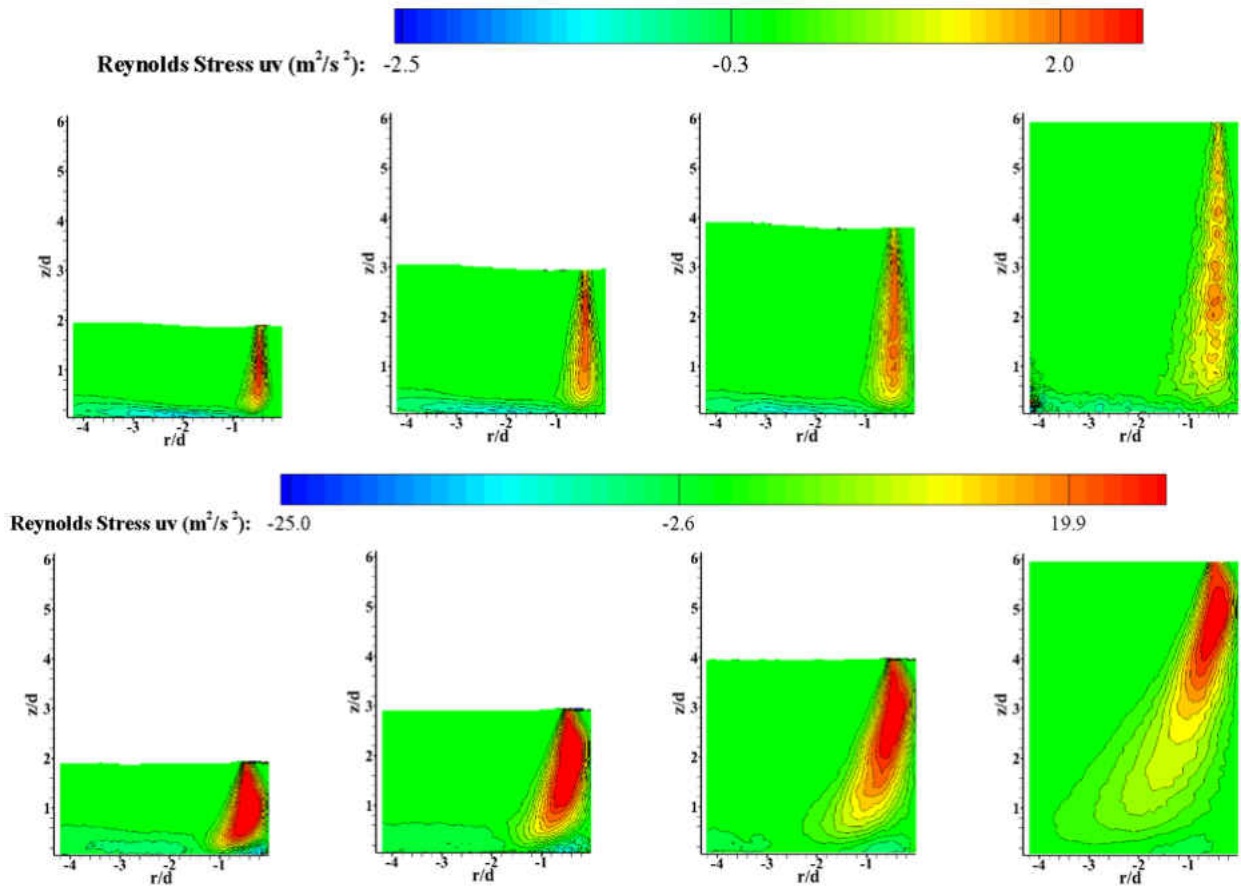


Figure 4.7: Reynolds Stresses for Baseline (Top) and Fluidic Oscillator (Bottom) for $z/d=2,3,4,6$ (Left to Right)

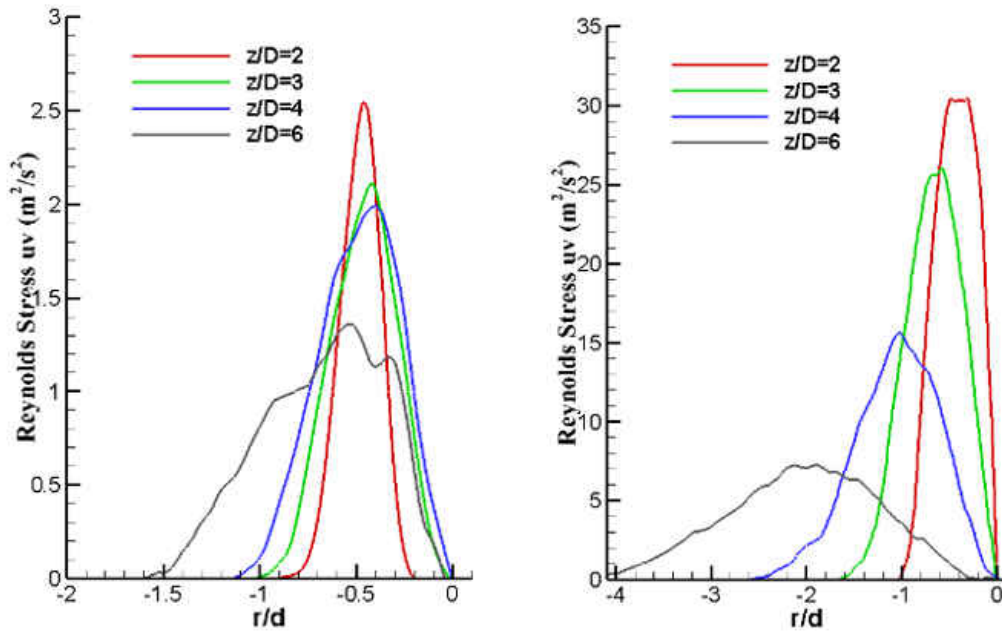


Figure 4.8: Reynolds Stresses, uv , Plotted at $z/d = 1$ for $z/d = 2,3,4,6$ for Baseline (Left) and FO (Right)

A further look into the Reynolds stresses closer to the surface show the magnitude of turbulence for a steady and sweeping jet in Figure 4.8. The baseline case demonstrates high turbulence close to the stagnation region while the fluidic oscillator expands radially much further. The peaks of the baseline case are relatively in the same area and of the same magnitude; however, the peaks of the fluidic oscillator shift away from the stagnation region as the z/d increases. This can again confirm the two lobes (with one peak seen in the figure) formed with a fluidic oscillator at higher z/d that is seen by Agricola [1] and seen in the flow field in Figure 4.1. Another thing to note is that most of the turbulence occurs in the stagnation zone.

4.2 Heat Transfer Results

Table 4.3 displays the test matrix used for the heat transfer study of the fluidic oscillator. In order to evaluate the performance of a sweeping jet, a reference case was utilized. This baseline

case has an identical setup to the companion fluidic oscillator case. Note the baseline case has an identical orifice shape as the exit throat of the fluidic oscillator, i.e. rectangular, with same hydraulic diameter, and cross sectional area resulting in an L/d of 1. Due to the physical constraints from the rig design, heat transfer at z/d of 2 was not tested and was studied only in the PIV results.

Table 4.3: Fluidic Oscillator Heat Transfer Matrix

Fluidic Oscillator Heat Transfer Testing Matrix				
Jet Case	Reynolds Number	z/d	Hydraulic Diameter, d (mm)	Other Parameters
Baseline	30,000	3, 4, 6	28	Confined/ Unconfined
FO	30,000	3, 4, 6	28	Confined/ Unconfined

To reiterate the parameters of a fluidic oscillator, the main interests are the sweeping angle and frequency which are adjusted in the fluidic oscillator geometry. These were selected based on a desired surface coverage and flow rate. The frequency of oscillation is defined as the time it takes for the jet to travel to the same location as the reference frame. The frequency of the fluidic oscillator is mostly influenced by the flow rate and pressure drop that is introduced from the jet stream separation forming in the mixing chamber by flow attachment to the walls. The sweeping angle changes how much coverage and the uniformity of heat removal on the surface which is introduced in the jet stream separation in the mixing chamber by flow attachment to the walls. The sweeping angle is affected by the pressure gradient across the jet exit and can impede the jet from moving laterally and not sweep enough to cover the surface, Camci [7].

Figure 4.9 and 4.10 depict the Nusselt number distribution for a confined and unconfined setup. The Nusselt number data shown is a normalized value using the baseline data for reference. The baseline cases shared the same trends for the confined and unconfined cases. The confined case had lower heat transfer for the baseline and fluidic oscillator. The same could be stated for the fluidic oscillator where the Nusselt number monotonically decrease with increasing z/d spacing. Considering the uncertainty of the experiment, it can be concluded that a minor heat transfer enhancement was seen for $z/d=2$. This leads to the possibility of varying the frequency of

the fluidic at the same flow rate to determine if this may benefit the heat transfer. It is clear from the heat transfer results that the confined cases generates recirculation around the jet and deteriorates the heat removal on the surface, which has been proven for the steady jet as well.

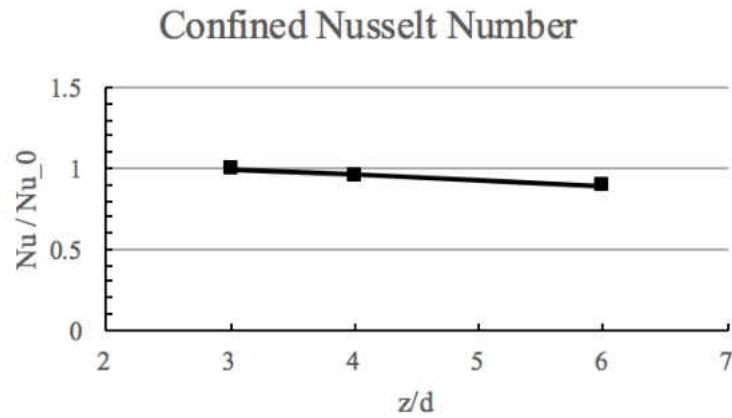


Figure 4.9: Normalized Nusselt Number for Baseline and Fluidic Oscillator for Confined Setup

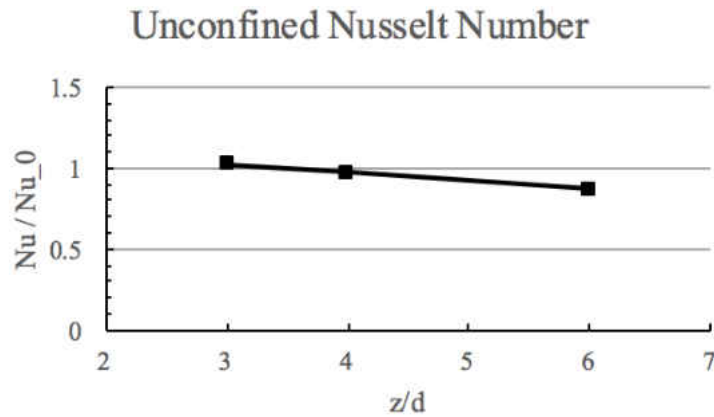


Figure 4.10: Normalized Nusselt Number for Baseline and Fluidic Oscillator for Unconfined Setup

Comparing the confined and unconfined cases as demonstrated in Figure 4.1 quantifies the effects of recirculation especially for a z/d of 3 where some enhancement is seen. The fluidic

oscillator yielded some enhancement over the associated steady jet with z/d of 3 unconfined having the highest heat transfer. The unconfined case at a z/d of 3 demonstrated to have an effect on the Nusselt number where recirculation may have deteriorated the jet before impingement instead of on the wall jet as expressed by Huber and Viskanta [24]. The importance of a dense boundary layer and high momentum jet are the keys for high heat transfer.

4.3 Summary of the Results

An experimental and numerical investigation of a sweeping jet for the use of heat transfer was studied for further insight on the effects of flow mechanisms on the heat transfer performance. This was studied for a single Reynolds number with varying jet-to-surface spacing, under confined and unconfined cases. The results are below:

- At a z/d of 2, the jet core of the oscillator was highly turbulent and a denser boundary layer based on the results from the Reynolds stresses, Figure 4.7, and boundary layer 4.5.
- Mean velocity fields at a z/d of 2 had no obvious stagnation zone for confined and unconfined. On the contrary, a less noticeable stagnation zone was seen for the higher jet to surface spacing.
- The boundary layer for confined and unconfined reflected the same profiles.
- Fluidic oscillator's heat transfer performance was the best for z/d of 3 and unconfined while a low heat transfer performance was seen for z/d of 4 and 6 in both confined and unconfined when compared to a rectangular slot orifice.
- Confined case had significant lower heat transfer compared to unconfined for z/d of 3 while there was insignificant influence for z/d of 4 or 6.

A fluidic oscillator may be optimized based on its applications. Although the area-averaged heat transfer deteriorates with a sweeping jet for a certain high jet-to-surface spacings, parameters

from an oscillator (such as sweeping angle, frequency, and internal design) would be of interest to study their impacts. Also, a sweeping jet results in a linear manner and may perform better for heat transfer if it was designed for a radial frame.

CHAPTER 5: ANALYSIS OF PULSING MECHANISM

The idea of a pulsating flow uses the notion of introducing a disturbance in the jet that would result in a transient boundary layer performance. To gather what would benefit the heat transfer, two parameters were considered in addition to the steady jet behavior from the pulsing setup. This mechanism would change the duty cycle and frequency of the jet exiting from the orifice plate. Meaning, the flow could be broken up (duty cycle) at different time periods (frequency). Nonetheless, literature collected and studied led to an understanding that it is possible to enhance the heat transfer of an impinging jet using an unsteady effect but there is no clear understanding of its heat transfer possibilities. The first important factor was to determine the major term affecting the flow. The testing matrix for all pulsing tests is shown in Table 5.1 where the Reynolds number is identical to the oscillator for later comparison.

Table 5.1: Pulsing Mechanism Matrix

Pulsing Mechanism Testing Matrix				
Reynolds Number	z/d	Jet Diameter, d (mm)	Duty Cycle (%)	Frequency (Hz)
30,000	3	30	27, 33, 50	20, 50, 100, 200, 300, 400

5.1 Flow Analysis Results

The flow field of the jet is considered turbulent at the point the discrete hot wire data was taken. To characterize the turbulence of the jet right at the exit, hot wire data is taken to investigate the eddies formed from the opening and closing of the jet as it interacts with the ambient flow. With this case of the velocity's magnitude, the velocity measured is the magnitude with no sense of direction of the flow. This is shown in equation 5.1 describing the measured velocity considers

all the directions of the flow.

$$U = u + v + w \quad (5.1)$$

The measured velocity over time records the mean velocity, \bar{U} , and turbulent component of velocity, $U'(t)$ where it is decomposed to:

$$U(t) = \bar{U} + U'(t) \quad (5.2)$$

Because the flow turbulence related to eddies are random, the turbulent motions are characterized using a statistical approach. The discrete data points, U_i , is a series of discrete data points that are averaged over time, noted with a bar, over a time interval. Equation 5.3 is the discrete mean velocity. Equation 5.4 is the same as Equation 5.2 re-written in terms of fluctuations for discrete points. Equation 5.5 is the root-mean-square of the velocity for a set of discrete points.

$$\bar{U} = \frac{1}{N} \sum_{i=1}^N U_i \quad (5.3)$$

$$U'_i = U_i - \bar{U} \quad (5.4)$$

$$U_{rms} = \sqrt{\frac{1}{N} \sum_{i=1}^N (U'_i)^2} \quad (5.5)$$

5.1.1 Mean Velocity and Turbulence

To quantify the fluctuations of the flow right at the exit of the jet, a radar chart plots the Strouhal number versus the enhancement of the heat transfer in Figure 5.1. It can be seen that a Strouhal number of 0.04, 0.22, and 0.45 higher enhancements. Thus, a flow property may be explained after a certain Strouhal number as explained by Hofmann [21]. It was observed in that

paper that vortices formed at the shear layer of a jet move along the jet and may enhance the heat transfer. However, this only occurs for a Strouhal number greater than 0.2 with a set residence time for the frequency of the pulsation to affect the heat transfer and boundary layer thickness. Anything below this Strouhal number according to the author is considered quasisteady flow. This hypothesis does not seem to hold true for the Strouhal number relative to Nusselt number since the Nusselt number was the highest for a Strouhal number at 0.04.

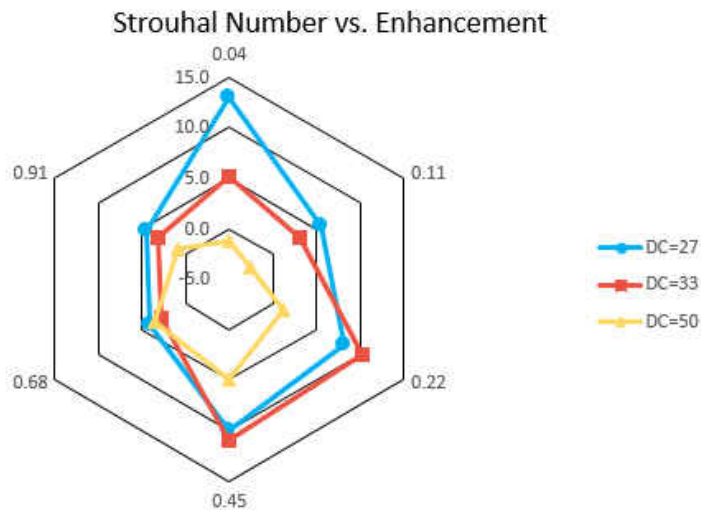


Figure 5.1: Strouhal Numbers for DC=27%, 33%, 50%

The frequencies tested in this matrix do not capture the natural frequency of the jet that would occur at roughly a Strouhal number of 1 which may have had a positive influence on heat transfer. If tested as the natural frequency of the jet, the vortex strength may be enhanced. To generate a second natural frequency vortex, the frequency of the jet should be set to half the natural frequency. This would ultimately produce larger but possibly weaker vortices that would lead to the pairing of these vortices [34].

The next item presented is the mean velocity and the rms values for the three duty cycles at all the frequencies in the matrix as shown in Figures 5.2 and 5.3. The coordinates for the pulsed

cases have differed where a z/d of 0 is right at the exit of the jet. These mean velocities are taken right at the exit of the jet referred as a $z/d=0$ as this would be the a jet that has not been disturbed by the ambient conditions for a magnitude type of measurement. The black line corresponding to a steady jet is used as a reference; however, the frequency was of course not varied. It is noticeable how a duty cycle of 50% has a relatively low mean velocity compared to a steady jet. This will be translated later in the heat transfer results. It is seen that a frequency of 20Hz, 50Hz, and 400Hz have a higher velocity relative to a steady jet for a duty cycle of 27%. This can be due to the pressure build-up occurring when the jet is fully closed. The pressure difference generated above the disk leads to a high momentum flow as it exits and impinges on the surface. At a frequency of 400 Hz, the velocity varies greatly from one duty cycle to another. Moving forward most of the attention will be focused on a duty cycle of 27% and 33% as the trends show an enhancement in velocity. The three main conclusions from the graph are: 27% had the highest velocities followed by 33% then 50%; generally a local maxima is seen at 20 Hz and 50 Hz and a local minima is seen at 300 Hz; and 27% duty cycle always had a higher velocity compared to baseline.

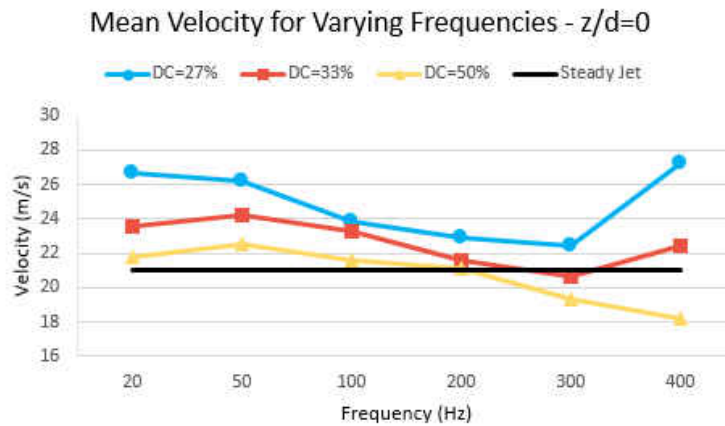


Figure 5.2: Mean Velocity for Reynolds Number=30,000 and $z/d=0$ for DC=27%, 33%, 50%

To consider the turbulence in the flow, a root-mean-square (rms) is calculated from the relative mean velocity. The typical rms value for the steady jet was ~ 1.7 . The least value as shown

in Figure 5.3 is 9.3. At a duty cycle of 27% and 33%, the rms values are much higher compared to a duty cycle of 50%. It also shows how certain frequencies excite the jet that can correspond to the heat transfer results. From this section, a general conclusion can be made how the duty cycle of 27% had the greatest deviations from a steady jet. This will be displayed when studying other data from the hot-wire results and heat transfer.

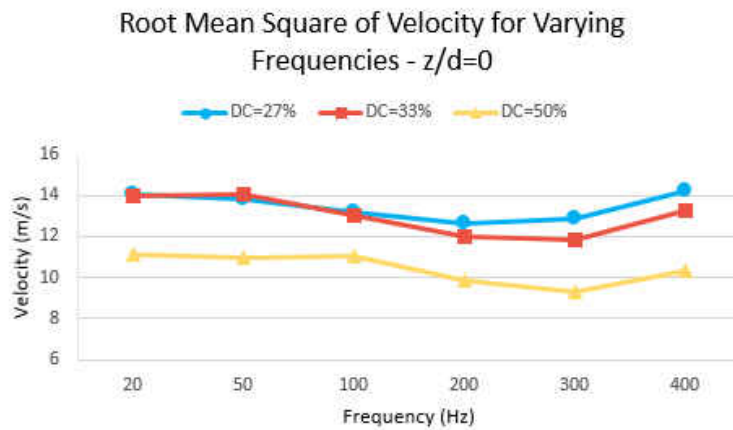


Figure 5.3: Root Mean Square of Mean Velocity for DC=27%, 33%, 50%

5.1.2 Duty Cycle - DC

To understand the flow exiting the orifice as a jet, the duty cycle, DC, is considered to characterize the amount of turbulence added to the flow. An example of one case is given in Figure 5.4 to show where the velocity corresponds in each case which is similar to Choutapalli [9] to visualize where the jet is opening and closing with respect to the disk. The numbers correspond to various times the jet is closing and opening and will be referred to as stages. Stage 1 is the jet fully closed as the duty cycle hole is not aligned. Stage 2 and 4 directs to the jet is slightly opened. Stage 3 is when the jet is fully opened as the DC hole is aligned with the jet.

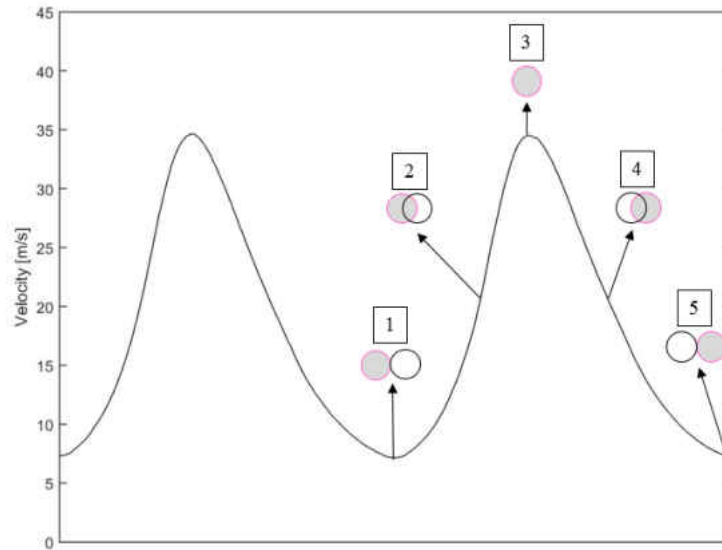


Figure 5.4: Opening Area Change During a Period. Shaded Circle: Jet Opening ; Open Circle: Disk Opening

A circular disk with circular jet holes would produce a velocity distribution similar to Figure 5.4. This varies depending on the duty cycle since the time the jet is closed increases with decreasing duty cycle. For all duty cycles, the velocity will be >0 for two observed reasons: leaking may have occurred between the duty cycle disk and the orifice plate as well as the hot-wire calibration uncertainty is high at lower velocities. Due to the wide-range of velocities encountered from the pulsing mechanism, the lower velocities were disregarded and the main focus was to capture the general profile of the duty cycles at various frequencies. Another note is the standard deviation shown in all figures representing duty cycle display a 95% confidence interval both low and high deviations.

In all images displayed representing the duty cycle, a 1-D interpolation FFT method is taken for 1 disk revolution. Interpolation FFT is defined as an interpolation of the Fourier transform of the function values in the velocity to produce equally spaced points. This was done to fit 10,000 points per revolution of the data taken. To smooth out the graphs, a moving average was done on

top of that for 100 points (which is =1% of the data being averaged). The settings for the duty cycle were kept constant for all images to properly compare the results. One point to note is the average velocity of a steady jet is roughly 21 m/s.

To start off with the lowest duty cycle considered at 27% in Figures 5.5 and 5.6, the lowest and highest frequency of 20 Hz and 400 Hz are compared, respectively. At stage 1, the jet is closed for a frequency at 20 Hz while flow is exiting at roughly 12 m/s for a frequency of 400 Hz. At stage 2, the air that was stagnant above the disk rapidly escapes for a frequency of 20 Hz while that pattern is not seen for 400 Hz. Stage 3, there is a maximum velocity of 52 m/s (roughly 2.5 times the average velocity of a steady jet) with the jet being fully opened. The peak is the same for both frequencies also reaching roughly the same velocity. The main point to notice is the amount of peaks and their corresponding velocities. At a duty cycle of 20 Hz, there are roughly 5 maximum peaks for one disk revolution. The interesting effect occurs at stage 4 where the flow is seen speeding up as the jet is coming to a complete close for a frequency of 20 Hz. The flow then comes to a stop as it reaches to stage 5 for the lower frequency. At a frequency of 400 Hz, it is clear that the velocity profile is smoother with the some peaks merging to form one maximum peak. In general, the jet experiences several disruptions as the disk opens and closes the jet forming a "packs" of air as it escapes from the orifice plate. The driving force with this duty cycle could be the pressure difference that builds up as the jet is closing and fully closed.

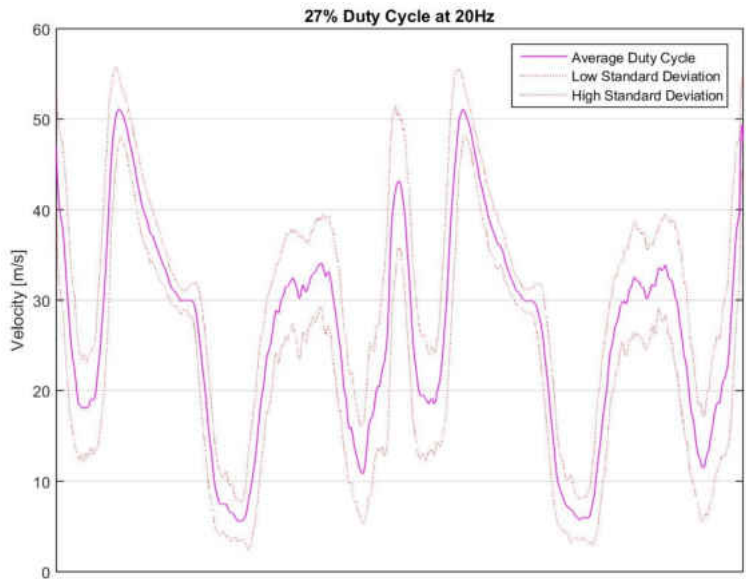


Figure 5.5: DC of 27% at a Frequency of 20 Hz

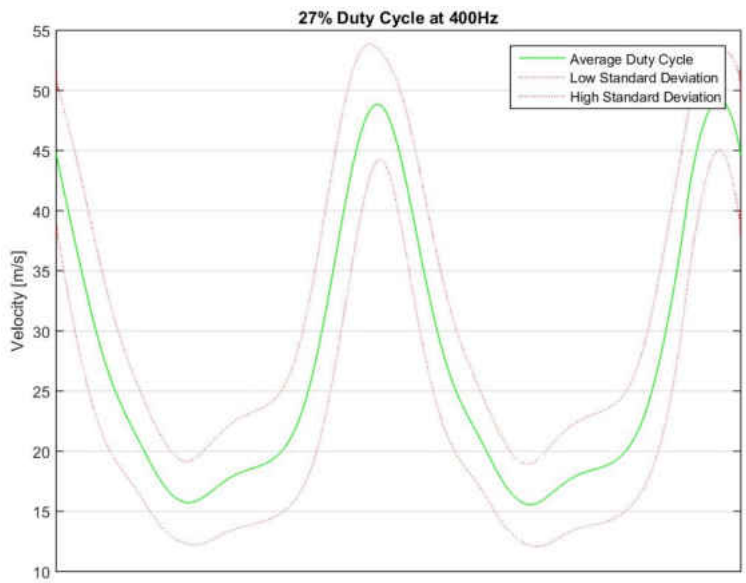


Figure 5.6: DC of 27% at a Frequency of 400 Hz

The next duty cycle of 33%, Figures 5.7 and 5.8 displays the same characteristics as the previous DC. This time it is more evident how there is a minimum and maximum peak

corresponding to the jet closing and opening. Stage 1 corresponds to a fully closed jet; however, the jet does not appear to come to a complete stop as flow is at approximately velocity of 8 m/s for a frequency of 20 Hz. The flow at 400 Hz reaches a higher velocity at the same stage leading to less of a pulsing effect. After that the stages are unclear at 2 and 3 where two peaks formed for a frequency of 20 Hz. It is unique for a frequency of 400 Hz to see a local maximum as the jet is opening at stage 2. Stage 3, corresponding to the maximum velocity in Figure 5.4, the peak is less defined for the lower frequency while the frequency of 400 Hz is visible. Stage 4 has a second local maximum peak at lower frequencies while the 400 Hz has a monotonically decreasing velocity. Stage 5 leads back to a decreasing to the same trend as in stage 1. The five peaks can be seen at a frequency of 20 Hz but their variation decreased meaning the jet momentum is less noticeable in this case.

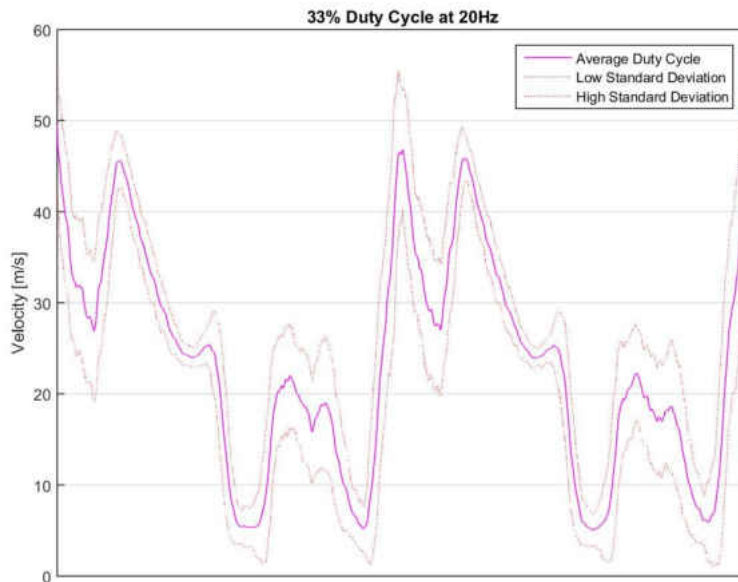


Figure 5.7: DC of 33% at a Frequency of 20 Hz

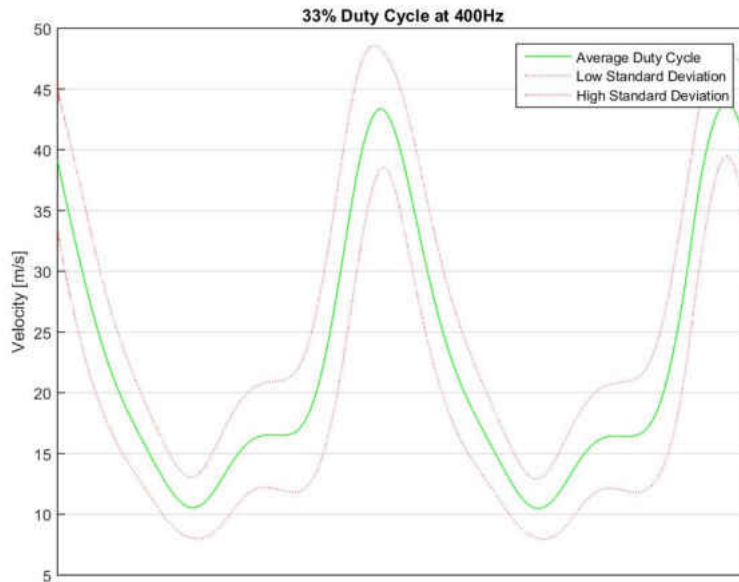


Figure 5.8: DC of 33% at a Frequency of 400 Hz

The last DC tested of 50%, the flow tends to slow down suggesting there is not much flow build up above the disk as it rotates shown in Figures 5.9 and 5.10. The maximum velocity being 40 m/s for a frequency of 20 Hz and a maximum velocity of 35 m/s for a frequency of 400 Hz. The velocity profiles at a frequency of 400 Hz is appearing as a sine wave with one clear maximum and minimum flow field. The peaks in the frequency of 20 Hz are less and that can give some understanding to why the heat transfer is higher for lower DCs. The pulsing behavior affects the heat transfer more when there is "packs" of fluid formed from continuous maximum and minimum velocities due to a difference in pressure above the disk. The number of peaks is decreased to 4 and the maximum peak is much less than the prior duty cycles.

Just from this section, it is difficult to tell which duty cycle would perform the best out of 27% and 33% but can be helpful when designing another duty cycle where the main goal would be to create high momentum flow that would produce a pulsing effect. The duty cycle at a $z/d=3$ is seen to be distributed and not much information can be extracted from the images.

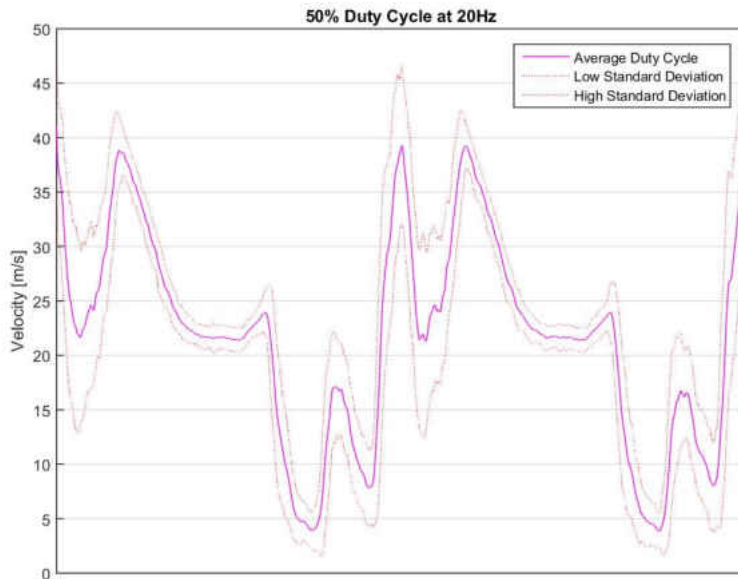


Figure 5.9: DC of 50% at a Frequency of 20 Hz

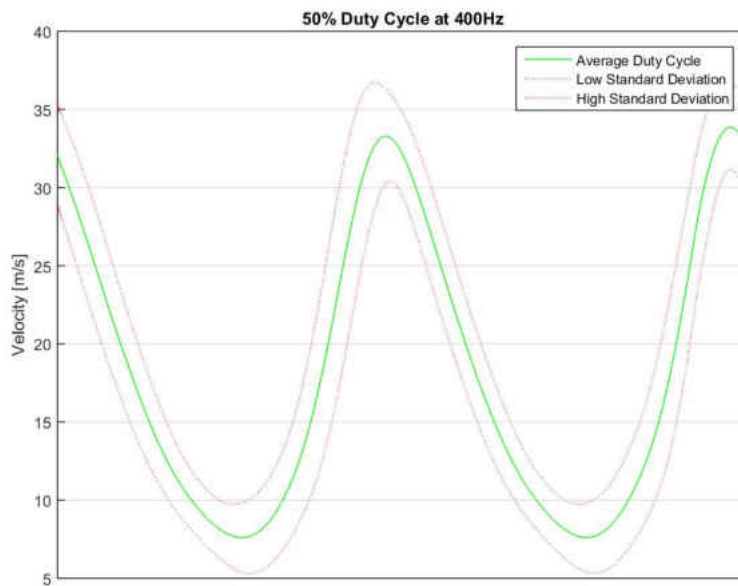


Figure 5.10: DC of 50% at a Frequency of 400 Hz

5.1.3 Power Spectral Density - PSD

This section delves into the strength of the vortices corresponding to the frequencies and duty cycles. The first comparison will be of the frequencies followed by the duty cycles. The power of the vortices is given by the absolute value of the Fast Fourier Transform, FFT, of the velocity data squared. The Fast Fourier Transform is obtained from MATLAB's software package. This is then divided by the number of data points, L , of the velocity to guarantee the power is independent of number of points as presented in Equation 5.6. This results in the Power Spectral density (PSD) of the flow that is a visual image representing the amount of energy the flow obtains.

$$Power = \frac{|FFT(U)|^2}{L} \quad (5.6)$$

The energy of the flow is the power divided by the sampling frequency as given in Equation 5.7. This is summarized by El-Gabry et al. [11].

$$Energy = \frac{Power}{F_s} \quad (5.7)$$

The energy of a steady jet is first explained then the energy for varying frequencies and duty cycles. If referred to as a $z/d=0$, this is located right at the exit of the jet. If referred to as $z/d=3$, this is located 3 jet diameters away from the exit of the jet. At the location of $z/d=3$, no impinging plate was placed to understand the jet characteristics, so it is a free jet - a typical jet loses its potential core after 4 or 5 jet diameters [4]. At a $z/d=0$ location, the flow has been undisturbed by the ambient flow; the jet's potential core is in contact and contains the most amount of energy. At a $z/d=3$ location, there is an exchange in momentum with the surrounding fluid [32] and the jet's principal frequencies will be noticed. The mean velocity profiles at the exit of the nozzle forming rectangular-shaped profile later turning into a bell-shape that may be described as a Gaussian distribution. The jet's frequency is designated as the speed the disk is rotating. For

example, a frequency of 20 Hz for any duty cycle applies to the disk spinning at 10 Hz from the disk containing two holes.

In Figures 5.11 and 5.12 depicts a steady jet's energy spectrum at the exit of the jet $z/d=0$ and a free jet at $z/d=3$ where the energy magnitude of the highest frequency is < 1 . The same case was tested at each DC for repeatability and possibly understand how the effects of the disk setup. A peak is seen at a frequency of ~ 1000 Hz where a natural frequency peak exists that produces a Strouhal number of roughly 1.4. Exciting the jet at this natural frequency may enhance the vortex strength consequently affecting the heat transfer [34].

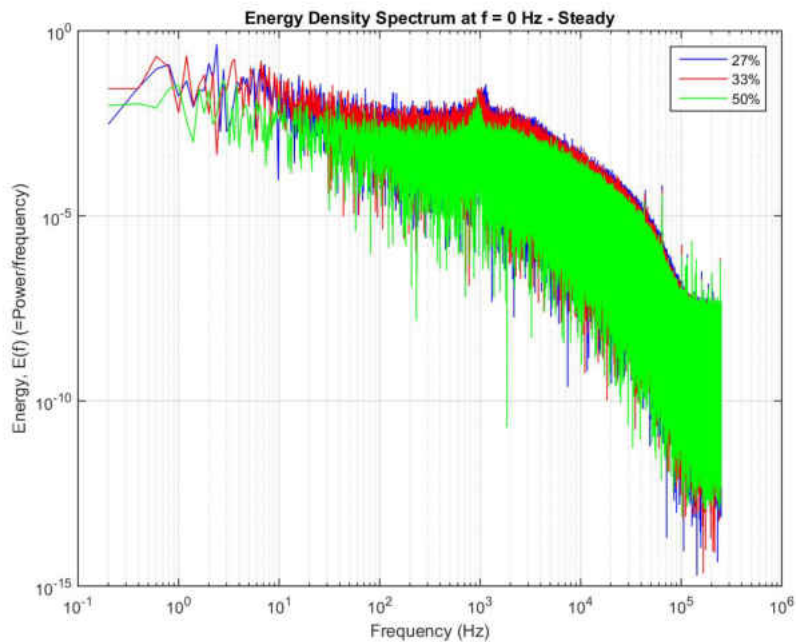


Figure 5.11: PSD of Steady Jet at a $z/d=0$

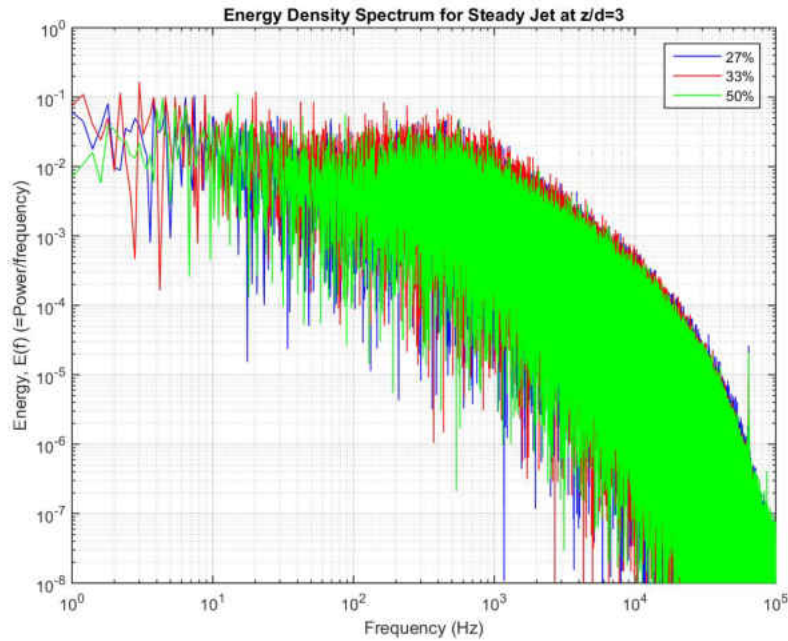


Figure 5.12: PSD of Steady Jet at a $z/d=3$

A further study of turbulence in a fully developed flow is the total kinetic energy of the flow. The fluctuating component of the jet's velocity can be broken down based on the eddies formed when the jet and ambient flow form a shear layer. The influence of the jet on the heat transfer is highly dependent on the strength and occurrence of the vortices formed. A quick description of understanding turbulent flow is provided by Hinze [18] that explains how turbulence has been quantified. It is explained how the energy-containing eddies make the main contribution to the total kinetic energy of the flow. This is displayed as the highest peaks in the PSD. Usually these eddies are associated to a wavenumber that indicates the range of the energy-containing eddies. The prime permanent eddies contain much less energy than the energy-containing eddies but are not small and can contain up to 20% of the total kinetic energy. Dissipation by viscous effects increases as the size of the eddies decrease. There is also a wavenumber associated with these eddies that is at the lower extreme of the wavenumber range. A decaying turbulence will occur if

the kinetic energy continuously decreases if there is no source of energy. The source of energy in this case can be considered the pressure difference formed from the disk opening and close the jet hole which transports the eddies on to the impinging surface. Moreover, the eddies related to the higher wavenumber - the energy containing eddies- are excited by the transfer of energy through inertia forces from the large eddies. To study these vortices from a pulsing jet, additional hot-wire data or PIV may provide this information.

In Figures 5.13 and 5.14 the energy spectrum for a constant duty cycle and varying frequency are compared. Looking at Figure 5.13, the three frequencies appear as the highest peaks, at 20, 50, and 100 Hz respectively. This corresponds the set frequency of the rotating disk which carry the highest magnitude of energy in all the flow. Comparing those three peaks, 20 Hz and 50 Hz are the maximum in magnitude. The flow's harmonic frequencies appear where a jet at 20 Hz will be have a harmonic frequency at the integer multiples of 40 Hz, 60 Hz, 80 Hz, so on and so forth. Surprisingly the highest energy - thus the highest peak- actually occurs at half the frequency of the jet. Meaning, a jet's frequency of 20 Hz will have the highest energy at a frequency of 10 Hz. This is unexpected and hard to understand what influences the jet. Moreover, this occurred for all frequencies tested where the highest peak is seen at half the jet's frequency. After that come the energy-containing eddies that are not associated with the flow's intended frequency which is visible for a frequency of 20 Hz. Smaller magnitude peaks occur in between these harmonic frequencies. This signifies how the flow's natural frequencies also contain high energy and could correlate to vortices formed at the exit of the nozzle.

Looking at Figure 5.14, the harmonic frequencies are noticeable as in the previous case. Another point is the balance of high and low peaks close to the main peaks which may signify the pulsing effect taking place. For a frequency of 300 Hz and 400 Hz, these harmonic frequencies continue to carry much energy. However, the lowest peaks corresponding to the slower flow begin to appear for a frequency of 300 Hz. This can be correlated later to the heat transfer results. Thus, at this frequency of 300 Hz, there may a change in flow behavior that is also seen in the steady jet

energy spectrum.

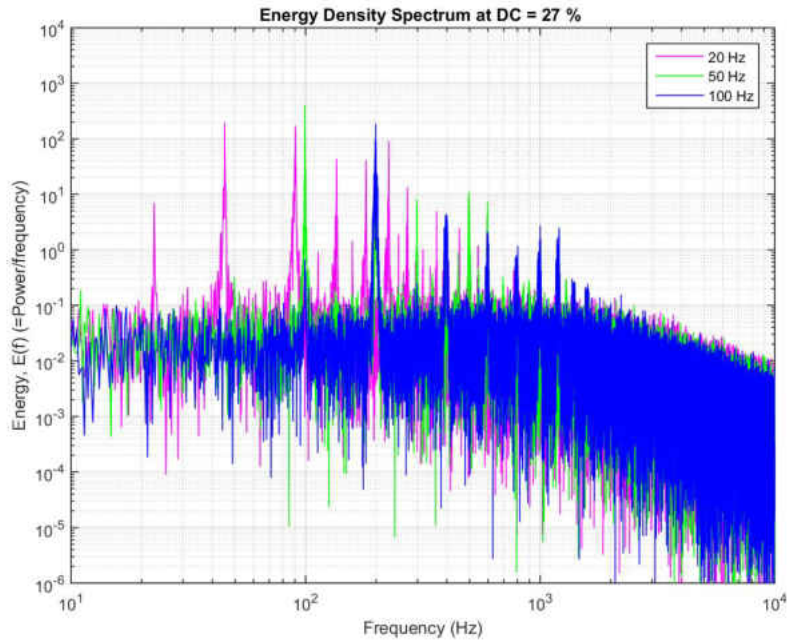


Figure 5.13: PSD for Frequencies of 20 Hz, 50 Hz, 100 Hz for a DC of 27%

Moving forward with a duty cycle of 33%, the amount of energy is relatively the same as prior. At a frequency of 20 Hz shown in Figure 5.15, a repeating pattern occurs, as in the previous duty cycle, and continue for the smaller energy-containing eddies. The amount of peaks increase at this duty cycle for frequencies of 20 Hz and 50 Hz. Nonetheless, the lower velocity flow peaks begin to appear quite early which can be an indication that the pulsing effect is decreasing. At the three higher frequencies shown in Figure 5.16, the peaks nevertheless contain the highest energy. At a frequency of 200 Hz, the flow becomes almost stagnant at lower frequencies. One hypothesis is that a counterbalance of high and low energy flow is what provides for higher heat transfer. Meaning, the flow comes to a relative stop and a high momentum flow then moves forward.

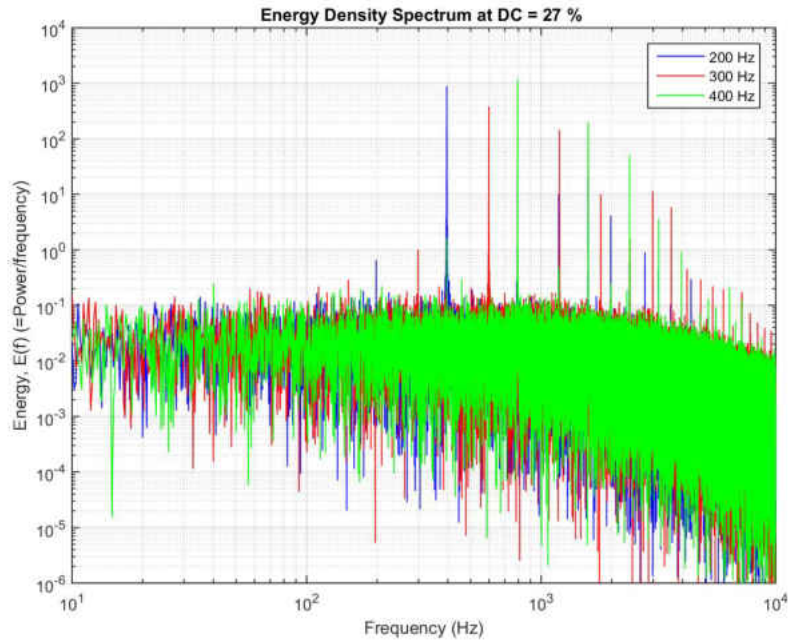


Figure 5.14: PSD for Frequencies of 200 Hz, 300 Hz, 400 Hz for a DC of 27%

The next duty cycle discussed of 50% is more disordered in contrast to duty cycle of 27% and 33% - Figures 5.17 and 5.18. At the lower frequencies tested, several peaks appear with the highest peaks still correlated to the flow's frequency. Conversely, smaller peaks appear before these three main frequencies. There is more chaos in the flow and the harmonic frequencies appear to be there. The slow velocity flow peaks appear more often. At the three higher frequencies tested of 200 Hz, 300 Hz, and 400 Hz, the three higher in magnitude peaks appear but the lower peaks show up in the general vicinity of these peaks.

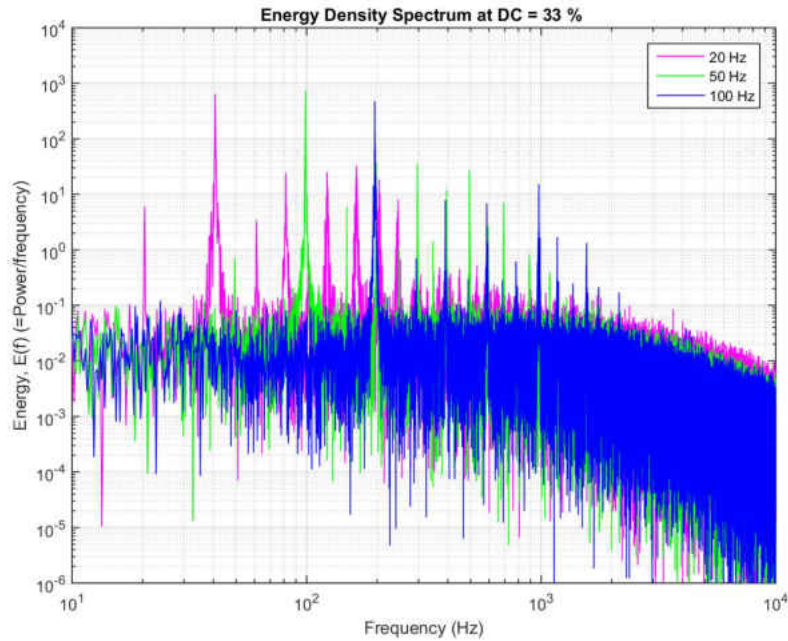


Figure 5.15: PSD for Frequencies of 20 Hz, 50 Hz, 100 Hz for a DC of 33%

In all pulsating cases a recurring pattern is seen independent of duty cycle and frequency: the energy contained in the jet is at least 100 times greater than a steady jet. The peaks corresponding to the jet's frequency contain the highest energy in all cases. A balance of high and low peaks seem to produce the best results in terms of heat transfer, as later discussed but kept in mind. The PSD of a free jet at a $z/d = 3$ is examined to understand how the jet's dominant frequencies that appear downstream of the jet's exit affect the heat transfer later.

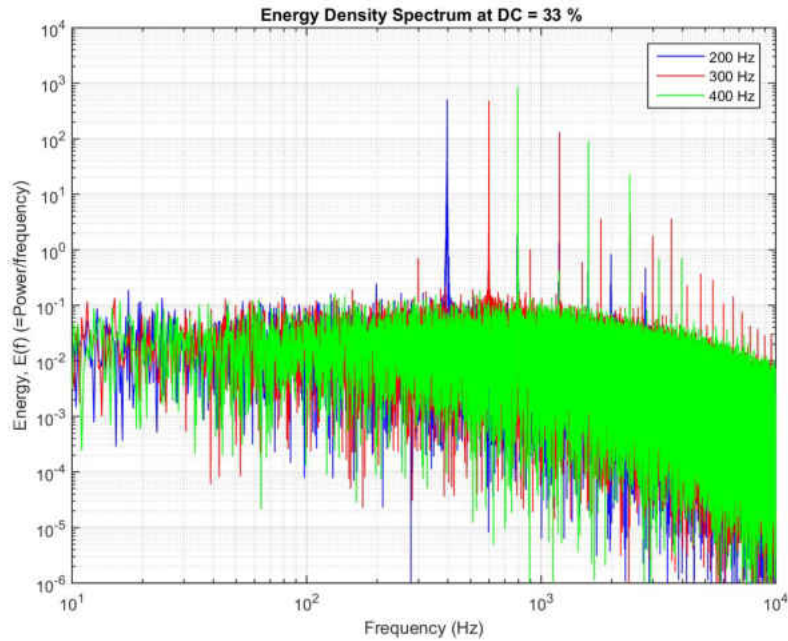


Figure 5.16: PSD for Frequencies of 200 Hz, 300 Hz, 400 Hz for a DC of 33%

Figures 5.19 and 5.20 show the same graphs at a $z/d=3$ where the impinging plate would be located. At the three lower frequencies, the 3 main peaks are clearly visible and maintain the same amount of energy. The smaller energy-containing eddies are not visible most likely due to their location changing. At the higher frequencies, the only main peak is visible at 200 Hz while the other two frequencies have decayed. The same point as explained previously is the balance of high and low peaks close to the main peaks. Their appearance is similar to a steady jet which will later be shown to have a major impact in heat transfer. Nonetheless, the energy contained at a frequency of 200 Hz is relatively much less than at the exit of the jet.

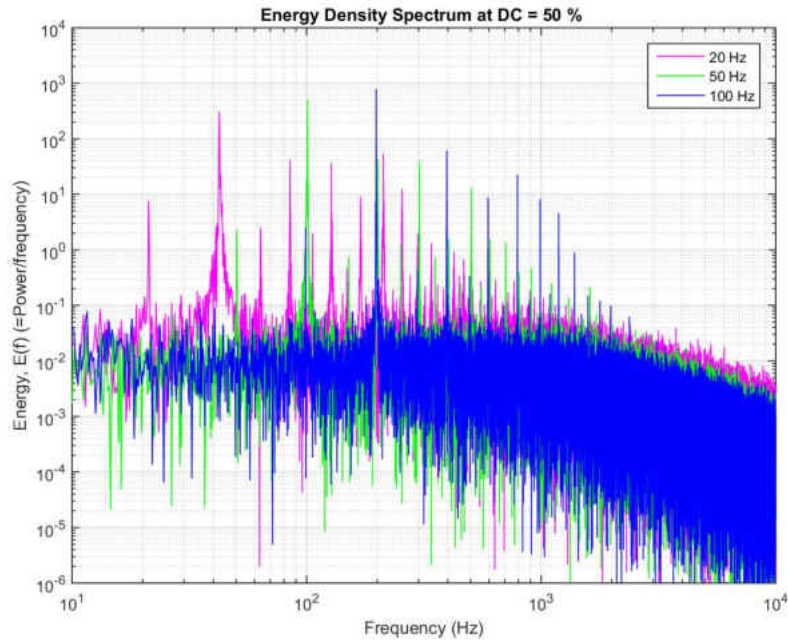


Figure 5.17: PSD for Frequencies of 20 Hz, 50 Hz, 100 Hz for a DC = 50%

Next is the 33% duty cycle in Figures 5.21 and 5.22. The main peaks for a frequency of 20 Hz and 50 Hz are visible and contain roughly the same amount of energy. This noticeable peak is not seen for a frequency of 100 Hz where much of the energy is lost. The same is said for the higher frequencies where a frequency of 200 Hz is contains roughly half of its previous amount while the 300 Hz and 400 Hz cases have decayed greatly.

At a duty cycle of 50% as shown in Figures 5.23 and 5.24, the pattern is repeated where the lower frequencies carry high energy and vice versa. The main peaks are clearly visible for all three frequencies of 20 Hz, 50 Hz, and 100 Hz surprisingly. At the higher frequencies, the flow is leading in the direction of a steady jet with a small peak for a frequency of 200 Hz.

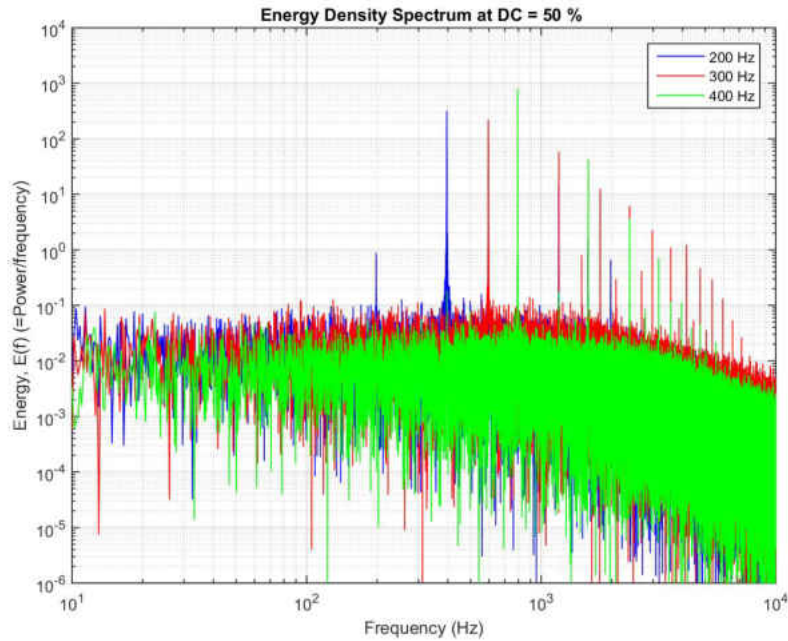


Figure 5.18: PSD for Frequencies of 200 Hz, 300 Hz, 400 Hz for a DC = 50%

The energy spectrum was studied to understand the eddies formed from the pulsing mechanism. Some information was gathered and can help explain the trends seen in the heat transfer results. It can be concluded that frequencies tested up to 200 Hz excite the jet and contribute to the mainstream jet turbulence at a jet-to-surface spacing of 3 when tested without an impinging plate. Thus, the surface at this spacing would mainly feel the effects of the jet turbulence caused by the pulsing mechanism. If the heat transfer analysis were not done it can still be said how the pulsing mechanism excites the jet and would be noticed even at a $z/d = 3$.

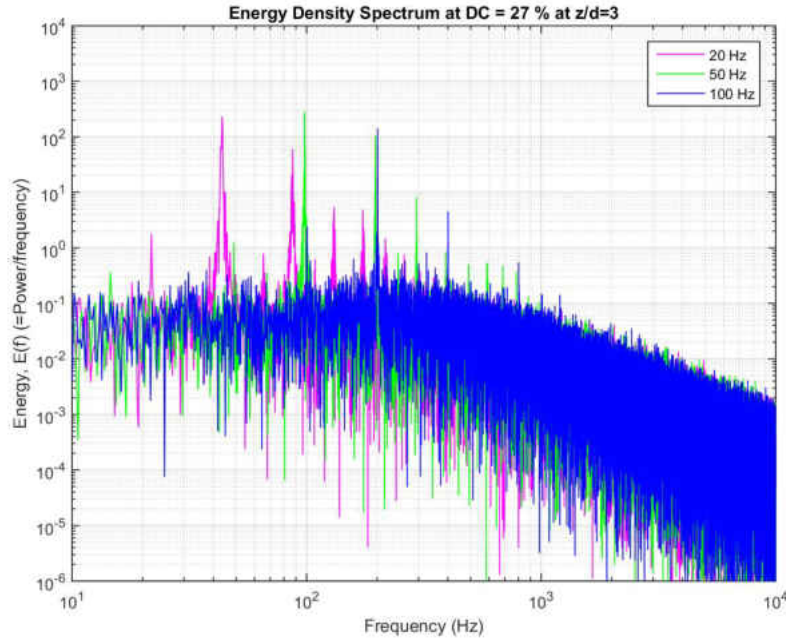


Figure 5.19: PSD for Frequencies of 20 Hz, 50 Hz, 100 Hz for a DC = 27% at a $z/d=3$

5.2 Heat Transfer Results

Further study of fluctuating flow using a pulsing mechanism was studied with copper block heat transfer. Keeping in mind that the jet shape is circular for the pulsation cases and square for the fluidic oscillator cases. With that being said, a baseline case was done for the pulsed case where a circular jet at a frequency of 0 Hz was conducted for comparison. As shown in Figure 3.9, all heat transfer tests were confined - a circular plate was placed flush to the jet exit. The Nusselt number data shown is a normalized value using the baseline data for reference. These tests were recorded at steady state signifying a temperature change (i.e. $\Delta T = T_{surface} - T_{jet}$) for a minimum of 10 minutes. The pulsating cases matrix is shown in Table 5.2.

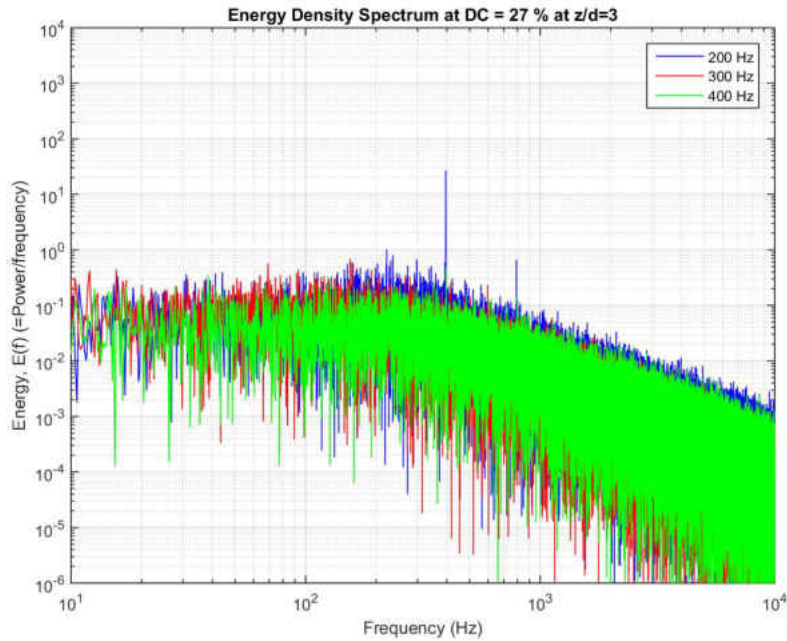


Figure 5.20: PSD for Frequencies of 200 Hz, 300 Hz, 400 Hz for a DC = 27% at a z/d=3

Table 5.2: Pulsed Flow Heat Transfer Test Matrix

Pulsed Flow Test Matrix				
Reynolds Number	z/d	Jet Diameter, d (mm)	Frequency (Hz)	Duty Cycle (DC)
30,000	3	30	20, 50, 100, 200, 300, 400	27%, 33%, 50%

The first result presented is at a duty cycle of 27% where the horizontal black line represents the frequency of 0 Hz or a steady jet. The vertical bars represent a +/- 9% error where no enhancement can be seen mostly due to the repeatability error. Therefore, the focus will be on the general trend of the results since it will be quite similar for all duty cycles. This trend being a high Nusselt number at the first frequency of 20 Hz then a peak at 200 Hz followed by a drop at 300 Hz.

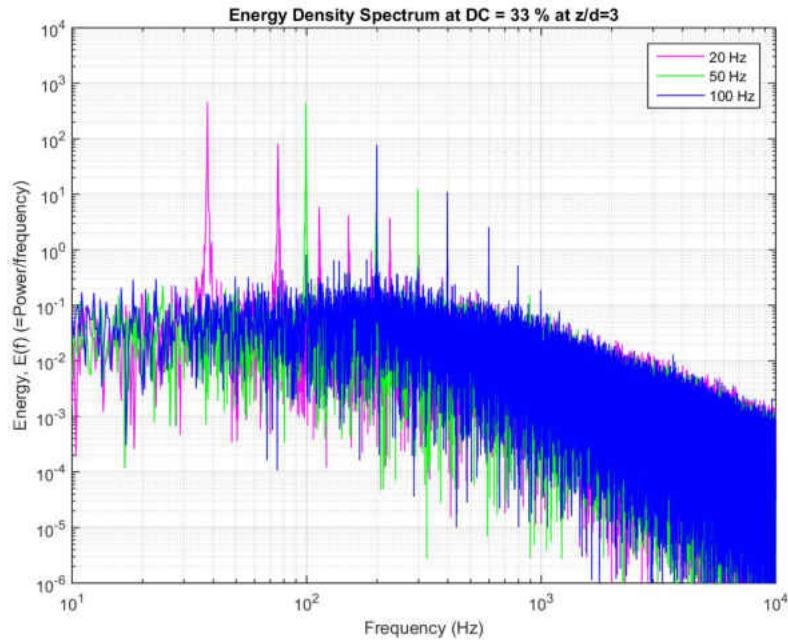


Figure 5.21: PSD for Frequencies of 20 Hz, 50 Hz, 100 Hz for a DC = 33% at a $z/d=3$

The same trend is seen for a duty cycle of 33% where there is a local minima at 50 Hz and 300 Hz presented in Figure 5.26. The general trend also decreased by a certain amount resulting in a decrease in Nusselt numbers for all frequencies. The general trend is again seen where a higher peak is seen at a frequency of 20 Hz and at 200 Hz. In this case, the 200 Hz test performs the best for this duty cycle. Yet, it is hard to say that an enhancement is seen for this data since the repeatability error is humongous.

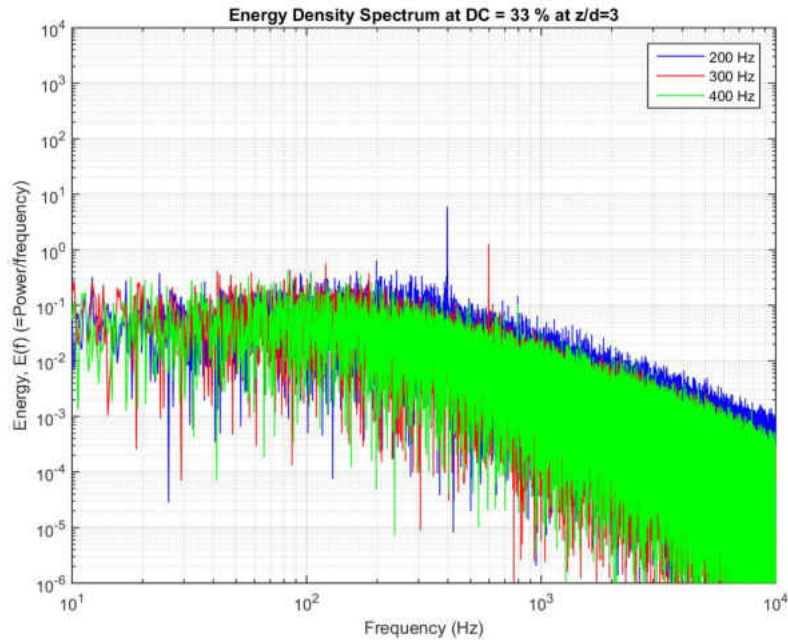


Figure 5.22: PSD for Frequencies of 200 Hz, 300 Hz, 400 Hz for a DC = 33% at a $z/d=3$

After that at a duty cycle of 50% shows a noticeable drop in Nusselt number proving to be the worst heat transfer result, Figure 5.27. The trend is still noticeable in this case where a local maximum is seen at 20 Hz and 200 Hz. Based on the PSD at this duty cycle and a $z/d=3$, it was expected for the heat transfer results to be very similar to the baseline case.

It can be noted that the pulsing effect on heat transfer is more effective for smaller duty cycles when comparing the data above. Another note is the hot-wire data resembled the results of the heat transfer with some doubt at 50 Hz where the trend was indifferent. Generally noting, a frequency of 20 Hz and 200 Hz proved to have the highest heat transfer results. The heat removal potential from a pulsed air jet is seen to be affected more by the duty cycle rather than the pulsed frequency based on the general trends. This was also seen by Marcum when testing different duty cycles and frequencies using a solenoid valve [31].

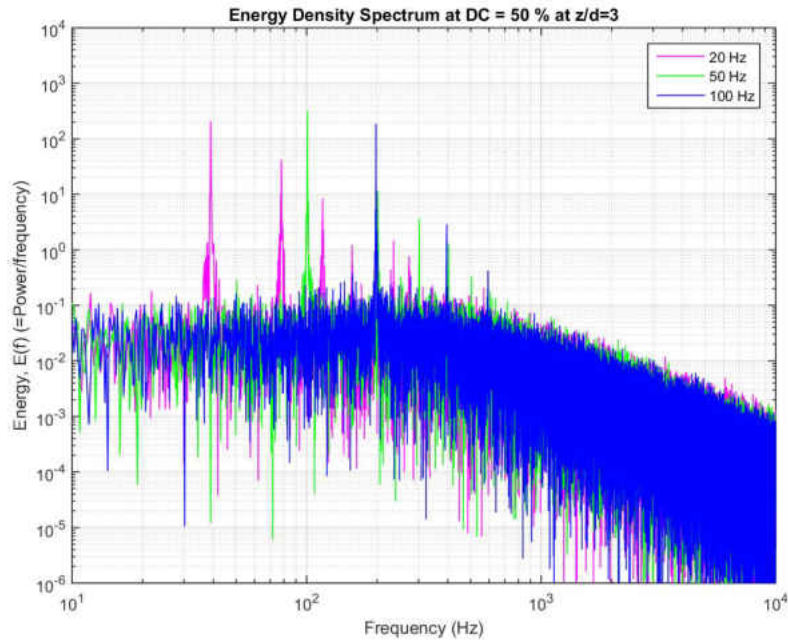


Figure 5.23: PSD for Frequencies of 20 Hz, 50 Hz, 100 Hz for a DC = 50% at a $z/d=3$

5.2.1 Additional Heat Transfer Data

Further testing was provided by Siemens where a study of varying the frequency for a given duty cycle is shown in Figure 5.28. Notes about these tests: the jet-to-surface spacing, z/d , is 2; duty cycle was 50%; and the Reynolds number was 34,000. Enhancement was seen up to 28% for a frequency of 280 Hz. This can be explained based on the eddies that form at the exit of the nozzle that produce an unsteady boundary layer at the surface as stated by Zuckerman [46].

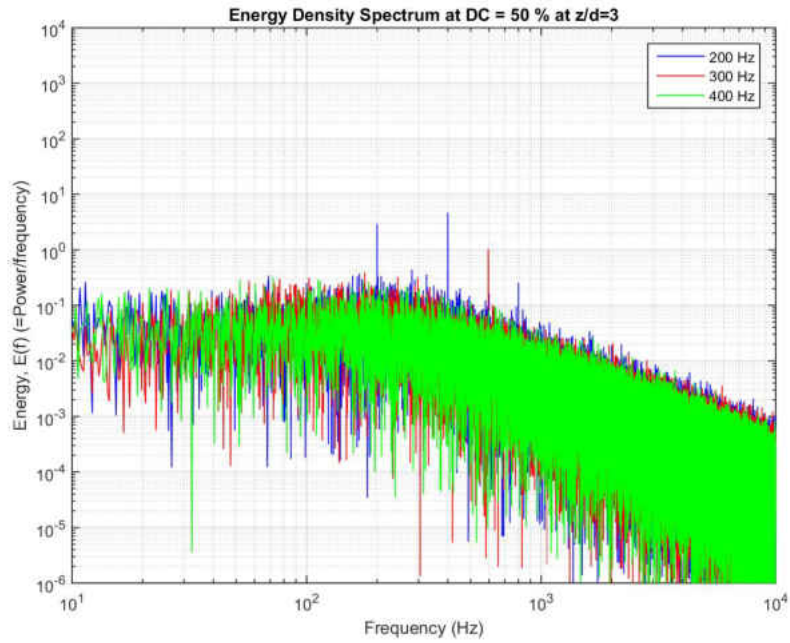


Figure 5.24: PSD for Frequencies of 200 Hz, 300 Hz, 400 Hz for a DC = 50% at a z/d=3

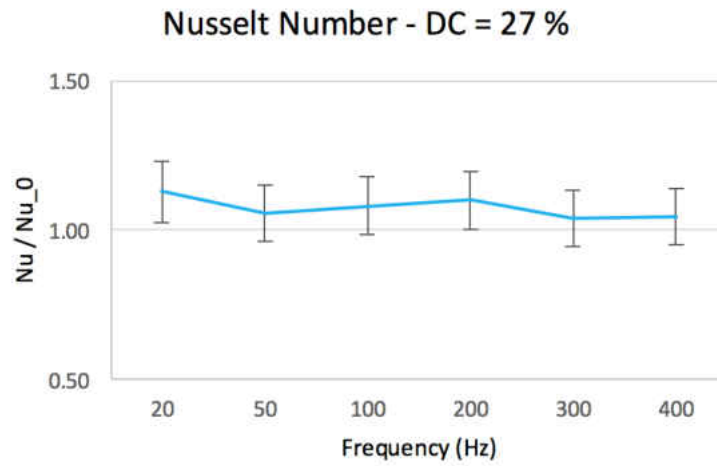


Figure 5.25: Nusselt Number Comparison of Baseline and DC = 27%

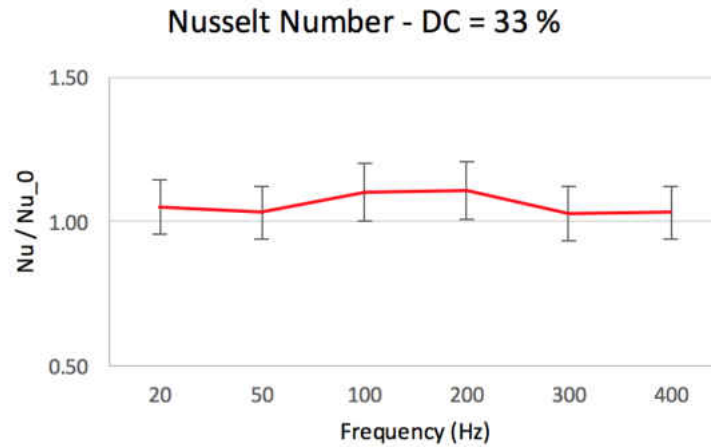


Figure 5.26: Nusselt Number Comparison of Baseline and DC = 33%

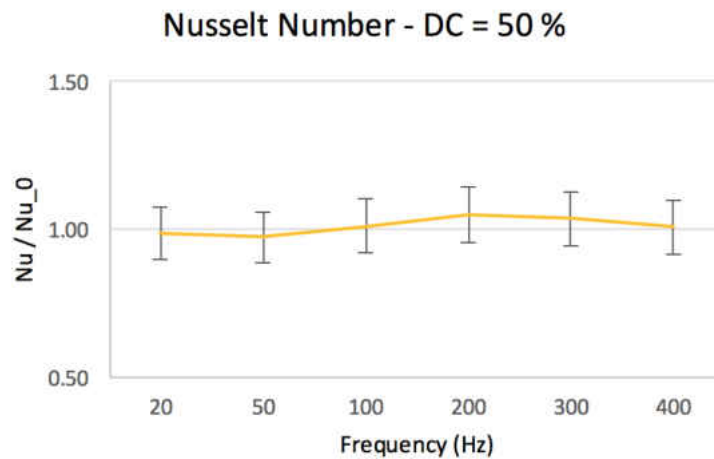


Figure 5.27: Nusselt Number Comparison of Baseline and DC = 50%

The trends are seen again with this graph where 20 Hz showed enhancement then a drop was seen for a frequency of 50 Hz and another local maximum peak at 280 Hz. This can be correlated to the Strouhal number that ranged from 0.04 - 1.22 where an optimal Strouhal number may produce the best results if matched with the natural frequency of the jet. Based on the conclusions previously studied, the results may have shown more enhancement if lower duty cycles

were tested. To compare the results, enhancement was seen for a duty cycle of 50% when the jet-to-surface spacing, z/d , was less. A conclusion can be made that generally the pulsing effect works better for lower jet-to-surface spacings.

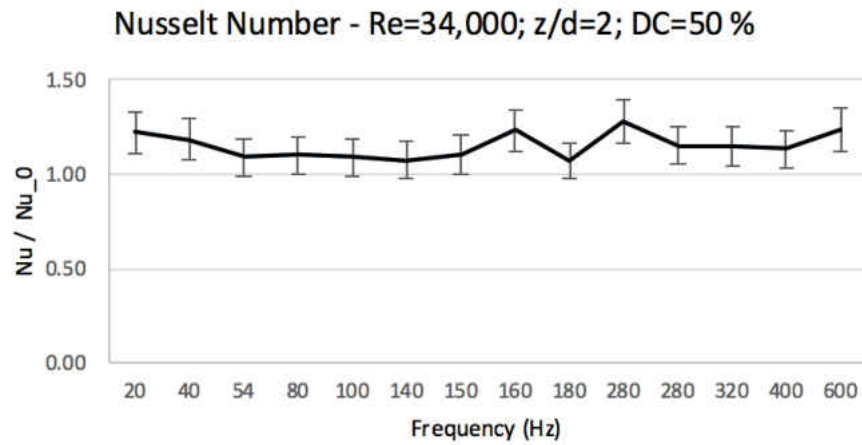


Figure 5.28: Nusselt Number Comparison of Baseline and DC = 50% for a Reynolds Number = 34,000 and $z/d=2$

5.3 Summary of the Results

The pulsing mechanism's goal was to understand how an unsteady jet would benefit the heat transfer relative to a steady jet. The parameters chosen to produce an unsteady jet in this case were duty cycle and frequency. To support the heat transfer results, the jet behaviour was characterized by using hot-wire on a steady and unsteady jet. From those results the data was generated to understand: the mean velocity and its fluctuations; duty cycle variances, and the energy spectrum distinctions.

- Mean velocity and turbulence: 27% had the highest velocities followed by 33% then 50%; generally all duty cycles had a local maxima is seen at 20 Hz and 50 Hz and a local minima is seen at 300 Hz; and 27% duty cycle always had a higher velocity compared to baseline.
- Duty cycle: The driving force with this duty cycle could be the pressure difference that builds up as the jet is closing and fully closed. The duty cycle of 27% contains high and low velocities in respect to one full revolution where there is 5 local maxima peaks and the maximum velocity is ~ 52 m/s. This behavior decays for a duty cycle of 50% where there are only 4 local maxima peaks and the maximum velocity is ~ 40 m/s.
- Power Spectral Density: The lower frequencies of 20 and 50 Hz showed maintained the high amounts of energy at both jet-to-surface spacings. While the higher frequencies decayed by the time the flow was at a $z/d=3$. A balanced amount of high and lower energy is necessary for the pulsing effect to be shown.
- Heat transfer: the general trend seen in the fluid results are seen in the heat transfer where most cases show a higher Nusselt number. At frequencies of 20 Hz and 200 Hz, there is a higher Nusselt number for all duty cycles. While at a frequency of 300 Hz, there is a drop in Nusselt number. The general trends show that the duty cycle may be more influential in the heat removal capabilities rather than the frequency. Based on the extra heat transfer data, the

pulsing mechanism does produce higher enhancement of up to 28% for certain frequencies and generally does better than a steady jet. Although the data was for a slight increase in Reynolds number, a duty cycle of 50% showed enhancement due to a decrease in jet-to-surface spacing. Thus, a duty cycle of 27% and 33% would have performed significantly better if tested at $z/d=2$ based on the conclusions from the mean velocity and turbulence section.

Using this information can prove that an unsteady jet has its pros and cons. It would be of large interest to move with an optimization of duty cycle as well as frequency. This can be done for varying Reynolds number and jet-to-surface spacings. The knowledge gained from this pulsed section can assist to design a stationary design that could replicate the results from here.

CHAPTER 6: CONCLUDING REMARKS AND FUTURE WORK

The present effort focused on understanding the fluid mechanics and heat transfer of novel, unsteady jet concepts. In this efforts, a fluidic oscillator and a pulsing mechanism were both considered. The direction of this work was strongly influenced by the literature discovered and the countless experiments in unsteady jets. Understanding turbulence, in itself, is continuously trying to be understood and predicted. The knowledge gained in this work is ever so slight compared to the spectrum of unsteady jets.

The main conclusions gathered from this work are: unsteady jets were measured to perform better than steady jets. Changing the parameters of a design greatly influence the results of the jet. An unsteady jet performs best when tested at lower jet-to-surface spacings but can be improved through optimization for various situations. A fluidic oscillator's strengths are mainly due to the sweeping angle and the frequency. The additional turbulence generated from the sweeping motion indeed helps the heat transfer. However, the flow's linear velocity profile may deteriorate the area-averaged Nusselt number on a circular surface. Therefore, designing another oscillator, as mentioned below, would be ideal. A pulsing mechanism's strengths are formed from the pressure difference occurring above the disk which dictates the amount of energy exiting the jet.

Future work inspired from this effort can be continued by designing a stationary oscillator that would be driven by a pressure difference. Knowing that the current fluidic oscillator sweeps in one direction and using the information gathered from the pulsed results would assist with designing an oscillator that would mimic the pulsing behavior. Future work may consider optimizing the pulsed results for a given Reynolds number and jet-to-surface spacing by decreasing the duty cycles and understanding the flow's natural frequencies to produce strong vortices that would impinge on the surface.

LIST OF REFERENCES

- [1] Lucas Agricola, Robin Prenter, Ryan Lundgreen, Mohammad Hossain, Ali Ameri, Jim Gregory, and Jeffrey Bons. Impinging sweeping jet heat transfer. In *53rd AIAA/SAE/ASEE Joint Propulsion Conference*, page 4974, 2017.
- [2] Ryoichi S Amano and Bengt Sundén. *Impingement jet cooling in gas turbines*, volume 25. WIT Press, 2014.
- [3] Robert P Benedict. *Fundamentals of temperature, pressure, and flow measurements*. John Wiley & Sons, 1984.
- [4] Garrett Birkhoff et al. *Jets, wakes, and cavities*, volume 2. Elsevier, 2012.
- [5] Bernhard C Bobusch, René Woszidlo, JM Bergada, C Navid Nayeri, and Christian Oliver Paschereit. Experimental study of the internal flow structures inside a fluidic oscillator. *Experiments in fluids*, 54(6):1559, 2013.
- [6] Hans H Bruun. *Hot-wire anemometry: principles and signal analysis*, 1996.
- [7] Cengiz Camci and Frank Herr. Forced convection heat transfer enhancement using a self-oscillating impinging planar jet. *Journal of heat transfer*, 124(4):770–782, 2002.
- [8] I Choutapalli, A Krothapalli, and JH Arakeri. An experimental study of an axisymmetric turbulent pulsed air jet. *Journal of Fluid Mechanics*, 631:23–63, 2009.
- [9] Issac Choutapalli. Effect of strouhal number on the flow field of a turbulent pulsed jet. In *2013 International Powered Lift Conference*, page 4378, 2013.
- [10] Tolga Demircan and Hasmert Turkoglu. The numerical analysis of oscillating rectangular impinging jets. *Numerical Heat Transfer, Part A: Applications*, 58(2):146–161, 2010.

- [11] Lamyaa A El-Gabry, Douglas R Thurman, and Philip E Poinsette. Procedure for determining turbulence length scales using hotwire anemometry. 2014.
- [12] Kazem Esmailpour, Mostafa Hosseinalipour, Behnam Bozorgmehr, and Arun S Mujumdar. A numerical study of heat transfer in a turbulent pulsating impinging jet. *The Canadian Journal of Chemical Engineering*, 93(5):959–969, 2015.
- [13] James Gregory and Mehmet N Tomac. A review of fluidic oscillator development. In *43rd AIAA Fluid Dynamics Conference*, page 2474, 2013.
- [14] James W Gregory, John P Sullivan, Ganesh Raman, and Surya Raghu. Characterization of the microfluidic oscillator. *AIAA journal*, 45(3):568–576, 2007.
- [15] B Han and RJ Goldstein. Jet-impingement heat transfer in gas turbine systems. *Annals of the New York Academy of Sciences*, 934(1):147–161, 2001.
- [16] Je-Chin Han, Sandip Dutta, and Srinath Ekkad. *Gas turbine heat transfer and cooling technology*. CRC Press, 2012.
- [17] Frank Herr and Cengiz Camci. Validation of an analytical model for an unsteady planar jet with self-sustained oscillations. In *Fluid Dynamics Conference*, page 2205, 1994.
- [18] J Hinze. 0. 1975 turbulence, 1976.
- [19] Justin D Hodges, Lauren Blanchette, Husam Zawati, Erik Fernandez, Jose Rodriguez, and Jayanta S Kapat. An experimental investigation of the flow field and heat transfer from a single impinging jet with varying confinement conditions. In *52nd AIAA/SAE/ASEE Joint Propulsion Conference*, page 5048, 2016.
- [20] Herbert Martin Hofmann, Matthias Kind, and Holger Martin. Measurements on steady state heat transfer and flow structure and new correlations for heat and mass transfer in submerged

- impinging jets. *International Journal of Heat and Mass Transfer*, 50(19-20):3957–3965, 2007.
- [21] Herbert Martin Hofmann, Daniela Luminita Movileanu, Matthias Kind, and Holger Martin. Influence of a pulsation on heat transfer and flow structure in submerged impinging jets. *International Journal of Heat and Mass Transfer*, 50(17-18):3638–3648, 2007.
- [22] Mohammad Arif Hossain, Robin Prenter, Lucas Agricola, Ryan K Lundgreen, Ali Ameri, James W Gregory, and Jeffrey P Bons. Effects of roughness on the performance of fluidic oscillators. In *55th AIAA Aerospace Sciences Meeting*, page 0770, 2017.
- [23] Chendong Huang and Rhyn H Kim. Three-dimensional analysis of partially open butterfly valve flows. *Journal of fluids engineering*, 118(3):562–568, 1996.
- [24] Aaron M Huber and Raymond Viskanta. Effect of jet-jet spacing on convective heat transfer to confined, impinging arrays of axisymmetric air jets. *International Journal of Heat and Mass Transfer*, 37(18):2859–2869, 1994.
- [25] K Jambunathan, E Lai, MA Moss, and BL Button. A review of heat transfer data for single circular jet impingement. *International journal of heat and fluid flow*, 13(2):106–115, 1992.
- [26] T Janetzke, W Nitsche, and J Täge. Experimental investigations of flow field and heat transfer characteristics due to periodically pulsating impinging air jets. *Heat and Mass Transfer*, 45(2):193–206, 2008.
- [27] Timm Janetzke and Wolfgang Nitsche. Time resolved investigations on flow field and quasi wall shear stress of an impingement configuration with pulsating jets by means of high speed piv and a surface hot wire array. *International Journal of Heat and Fluid Flow*, 30(5):877–885, 2009.

- [28] Takeyoshi Kimura, Takaharu Tanaka, Kayo Fujimoto, and Kazuhiko Ogawa. Hydrodynamic characteristics of a butterfly valve—prediction of pressure loss characteristics. *ISA transactions*, 34(4):319–326, 1995.
- [29] Tianshu Liu and JP Sullivan. Heat transfer and flow structures in an excited circular impinging jet. *International Journal of Heat and Mass Transfer*, 39(17):3695–3706, 1996.
- [30] Ryan K Lundgreen, Mohammad Arif Hossain, Robin Prenter, Jeffrey P Bons, James W Gregory, and Ali Ameri. Impingement heat transfer characteristic of a sweeping jet. In *55th AIAA Aerospace Sciences Meeting*, page 1535, 2017.
- [31] WR Marcum, SR Cadell, and C Ward. The effect of jet location and duty cycle on the fluid mechanics of an unconfined free jet and its heat transfer on an impinging plate. *International Journal of Heat and Mass Transfer*, 88:470–480, 2015.
- [32] Holger Martin. Heat and mass transfer between impinging gas jets and solid surfaces. In *Advances in heat transfer*, volume 13, pages 1–60. Elsevier, 1977.
- [33] Sreekant Narumanchi, Kenneth Kelly, Mark Mihalic, Shridhar Gopalan, Russ Hester, and Andreas Vlahinos. Single-phase self-oscillating jets for enhanced heat transfer. In *Semiconductor Thermal Measurement and Management Symposium, 2008. Semi-Therm 2008. Twenty-fourth Annual IEEE*, pages 154–162. IEEE, 2008.
- [34] TS O’Donovan and DB Murray. Heat transfer to an acoustically excited impinging air jet. In *Proceedings of the 5th European Thermal-Sciences Conference*, 2008.
- [35] Florian Ostermann, Rene Woszidlo, C Nayeri, and Christian O Paschereit. Experimental comparison between the flow field of two common fluidic oscillator designs. In *53rd AIAA aerospace sciences meeting*, page 0781, 2015.

- [36] RH Page, PS Chinnock, and J Seyed-Yagoobi. Self-oscillation enhancement of impingement jet heat transfer. *Journal of thermophysics and heat transfer*, 10(2):380–382, 1996.
- [37] Tim Persoons, Kuanysh Balgazin, Karl Brown, and Darina B Murray. Scaling of convective heat transfer enhancement due to flow pulsation in an axisymmetric impinging jet. *Journal of Heat Transfer*, 135(11):111012, 2013.
- [38] Tim Persoons, Alan McGuinn, and Darina B Murray. A general correlation for the stagnation point nusselt number of an axisymmetric impinging synthetic jet. *International Journal of Heat and Mass Transfer*, 54(17-18):3900–3908, 2011.
- [39] Czeslaw O Popiel and Olev Trass. Visualization of a free and impinging round jet. *Experimental Thermal and Fluid Science*, 4(3):253–264, 1991.
- [40] Ganesh Raman and Surya Raghu. Cavity resonance suppression using miniature fluidic oscillators. *AIAA journal*, 42(12):2608–2612, 2004.
- [41] David J Sailor, Daniel J Rohli, and Qianli Fu. Effect of variable duty cycle flow pulsations on heat transfer enhancement for an impinging air jet. *International Journal of Heat and Fluid Flow*, 20(6):574–580, 1999.
- [42] HS Sheriff and DA Zumbrennen. Local and instantaneous heat transfer characteristics of arrays of pulsating jets. *Journal of heat transfer*, 121(2):341–348, 1999.
- [43] Hermann Viets. Flip-flop jet nozzle. *AIAA journal*, 13(10):1375–1379, 1975.
- [44] L Wang, XG Song, and YC Park. Dynamic analysis of three-dimensional flow in the opening process of a single-disc butterfly valve. *Proceedings of the Institution of Mechanical Engineers, Part C: Journal of Mechanical Engineering Science*, 224(2):329–336, 2010.

- [45] Xin Wen, Yingzheng Liu, and Hui Tang. Unsteady behavior of a sweeping impinging jet: Time-resolved particle image velocimetry measurements. *Experimental Thermal and Fluid Science*, 96:111–127, 2018.
- [46] N Zuckerman and N Lior. Jet impingement heat transfer: physics, correlations, and numerical modeling. *Advances in heat transfer*, 39:565–631, 2006.
- [47] R Zulkifli and K Sopian. Studies on pulse jet impingement heat transfer: flow profile and effect of pulse frequencies on heat transfer. *Int. J. Eng. Technol*, 4(1):86–94, 2007.
- [48] Rozli Zulkifli, Kamaruzzaman Sopian, Shahrir Abdullah, and Mohd Sobri Takriff. Comparison of local nusselt number between steady and pulsating jet at different jet reynolds number. *WSEAS Transactions on Environment and Development*, 5(5):384–393, 2009.